AFRL-AFOSR-VA-TR-2024-0132

Non-Hermitian Topological Photonics

Zhen, Bo
TRUSTEES OF THE UNIVERSITY OF PENNSYLVANIA
3451 WALNUT ST
PHILADELPHIA, PA,
US

01/26/2024
Final Technical Report

Air Force Research Laboratory
Air Force Office of Scientific Research
Arlington, Virginia 22203
Air Force Materiel Command

REPORT DOCUMENTATION PAGE

PLEASE DO NOT RETURN YOUR FORM TO THE ABOVE ORGANIZATION.

1. REPORT DATE	2. REPORT TYPE	3. DATES COVERED	
20240126	Final	START DATE 20180215	END DATE 20220214

4. TITLE AND SUBTITLE
Non-Hermitian Topological Photonics

5a. CONTRACT NUMBER	5b. GRANT NUMBER	5c. PROGRAM ELEMENT NUMBER
	FA9550-18-1-0133	61102F
5d. PROJECT NUMBER	**5e. TASK NUMBER**	**5f. WORK UNIT NUMBER**

6. AUTHOR(S)
Bo Zhen

7. PERFORMING ORGANIZATION NAME(S) AND ADDRESS(ES)
TRUSTEES OF THE UNIVERSITY OF PENNSYLVANIA
3451 WALNUT ST
PHILADELPHIA, PA
US

8. PERFORMING ORGANIZATION REPORT NUMBER

9. SPONSORING/MONITORING AGENCY NAME(S) AND ADDRESS(ES)	10. SPONSOR/MONITOR'S ACRONYM(S)	11. SPONSOR/MONITOR'S REPORT NUMBER(S)
Air Force Office of Scientific Research 875 N. Randolph St. Room 3112 Arlington, VA 22203	AFRL/AFOSR RTB1	AFRL-AFOSR-VA-TR-2024-0132

12. DISTRIBUTION/AVAILABILITY STATEMENT
A Distribution Unlimited: PB Public Release

13. SUPPLEMENTARY NOTES

14. ABSTRACT
To explore topological phases in non-Hermitian photonic systems, with a focus on the non-Hermiticity induced by nonlinear optical parametric processes.

15. SUBJECT TERMS

16. SECURITY CLASSIFICATION OF:			17. LIMITATION OF ABSTRACT	18. NUMBER OF PAGES
a. REPORT	b. ABSTRACT	c. THIS PAGE		
U	U	U	UU	34

19a. NAME OF RESPONSIBLE PERSON	19b. PHONE NUMBER *(Include area code)*
ARJE NACHMAN	426-8427

Standard Form 298 (Rev.5/2020)
Prescribed by ANSI Std. Z39.18

AFOSR YIP Grant Final Report

Objective: To explore topological phases in non-Hermitian photonic systems, with a focus on the non-Hermiticity induced by nonlinear optical parametric processes.

Results:

1. **Observation of bulk Fermi arc and polarization half charges from paired exceptional points (Science 359, 1009, 2018)**

In recent years, topological effects have been widely explored in closed and lossless systems, where the physics is characterized by a Hermitian operator that ensures a real energy spectrum and a complete, orthogonal set of eigenfunctions. This has revealed a number of previously unknown phenomena such as topologically nontrivial band structures, and promising applications including backscattering-immune transport. However, most systems, particularly in photonics, are generically non-Hermitian because of radiation into open space or material gain or loss. Non-Hermiticity enables even richer topological properties, often with no counterpart in Hermitian frameworks. One such example is the emergence of a new class of degeneracies, commonly referred to as exceptional points (EPs), where two or more resonances of a system coalesce in both eigenvalues and eigenfunctions. So far, isolated EPs in parameter space and continuous rings of EPs in momentum space have been studied across different wave systems because of their intriguing properties, such as unconventional transmission or reflection and relations to parity-time symmetry as well as their unique applications in sensing and single-mode lasing.

We theoretically design and experimentally realize a new configuration of isolated EP pairs in momentum space, which allows us to reveal topological signatures of EPs in the band structure and far-field polarization, and to extend topological band theory into the realm of non-Hermitian systems. Specifically, we demonstrate that a Dirac point (DP) with nontrivial Berry phase can split into a pair of EPs when radiation loss—a form of non-Hermiticity—is added to a two-dimensional (2D)–periodic photonic crystal (PhC) structure. The EP-pair generates a distinct double–Riemann sheet topology in the complex band structure, which leads to two notable consequences: bulk Fermi arcs and polarization half topological charges. First, we demonstrate that this pair of EPs is connected by an open-ended isofrequency contour—a bulk Fermi arc—in direct contrast to the common intuition that isofrequency contours are necessarily closed loops. The bulk Fermi arc here is a special topological signature of non-Hermitian effects in paired EPs and resides in the bulk dispersion of a 2D system. This is fundamentally different from the previously known surface Fermi arcs that arise from the 2D projection of Weyl points in 3D Hermitian systems. Moreover, we find experimentally that around the Fermi arc, the far-field polarization of the system exhibits a robust half-integer winding

number, analogous to the orientation reversal on a Möbius strip. We show that this is a direct consequence of the topological band-switching properties across the Fermi arc connecting the EP pair and is direct experimental proof of the topological index associated with an EP. With comprehensive comparisons between analytical models, numerical simulations, and experimental measurements, our results are a direct validation of non-Hermitian topological band theory and present its novel application to the field of singular optics.

Our scheme involves splitting a single DP into a pair of EPs, which directly leads to the emergence of a bulk Fermi arc. First, consider a 2D-periodic PhC with a square lattice of circular air holes introduced into a dielectric material. In this Hermitian system (no material gain, loss, or radiation loss), the crystalline symmetry () ensures a quadratic band degeneracy at the center of the Brillouin zone . As this symmetry is broken, e.g., by shearing the structure into a rhombic lattice with elliptical holes, the quadratic degeneracy point splits into a pair of DPs situated at along the axis. The same splitting behavior is shown in both analytical models and numerical simulations.

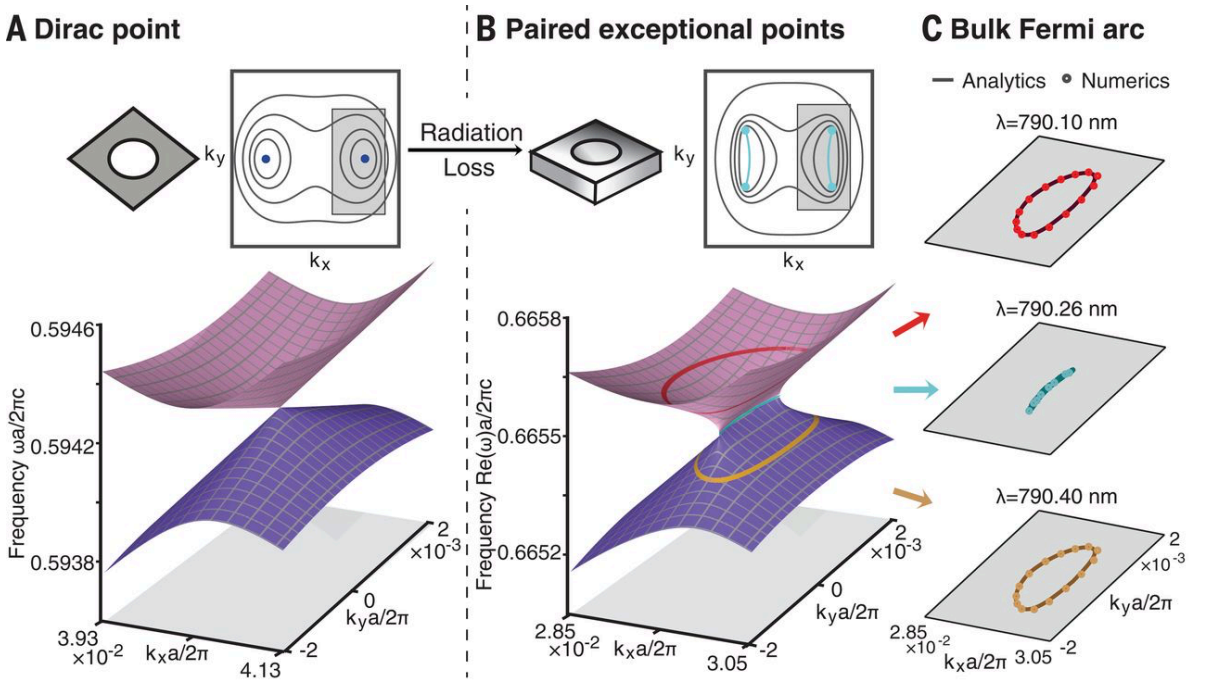

Fig. 1 Bulk Fermi arc arising from paired exceptional points split from a single Dirac point. (**A** and **B**) Illustration of photonic crystal (PhC) structures, isofrequency contours, and band structures. (A) Band structure of a 2D-periodic PhC consisting of a rhombic lattice of elliptical air holes, featuring a single Dirac point on the positive axis. (B) The real part of the eigenvalues of an open system consisting of a 2D-periodic PhC slab with finite thickness, where resonances experience radiation loss. The Dirac point splits into a pair of exceptional points (EPs). The real part of the eigenvalues is degenerate along an open-ended contour—the bulk Fermi arc (blue line)—connecting the pair of EPs. (**C**) Examples of the isofrequency contours in this system, including the open bulk Fermi arc at the EP frequency (middle panel), and closed contours at higher (upper panel) or lower (lower panel) frequencies. Solid lines are from the analytical model, and circles are from numerical simulations.

To experimentally demonstrate the bulk Fermi arc, we use interference lithography to fabricate PhC slabs in Si3N4 on top of a silica substrate. The PhC structure consists of rhombic unit cells with side length nm, unit cell angle , and elliptical air holes with long-axis length nm and short-axis length nm. Scanning electron microscope (SEM) images of the fabricated samples are shown below. The structure is immersed in an optical liquid with refractive index matched to that of the silica substrate to create an up-down symmetric environment.

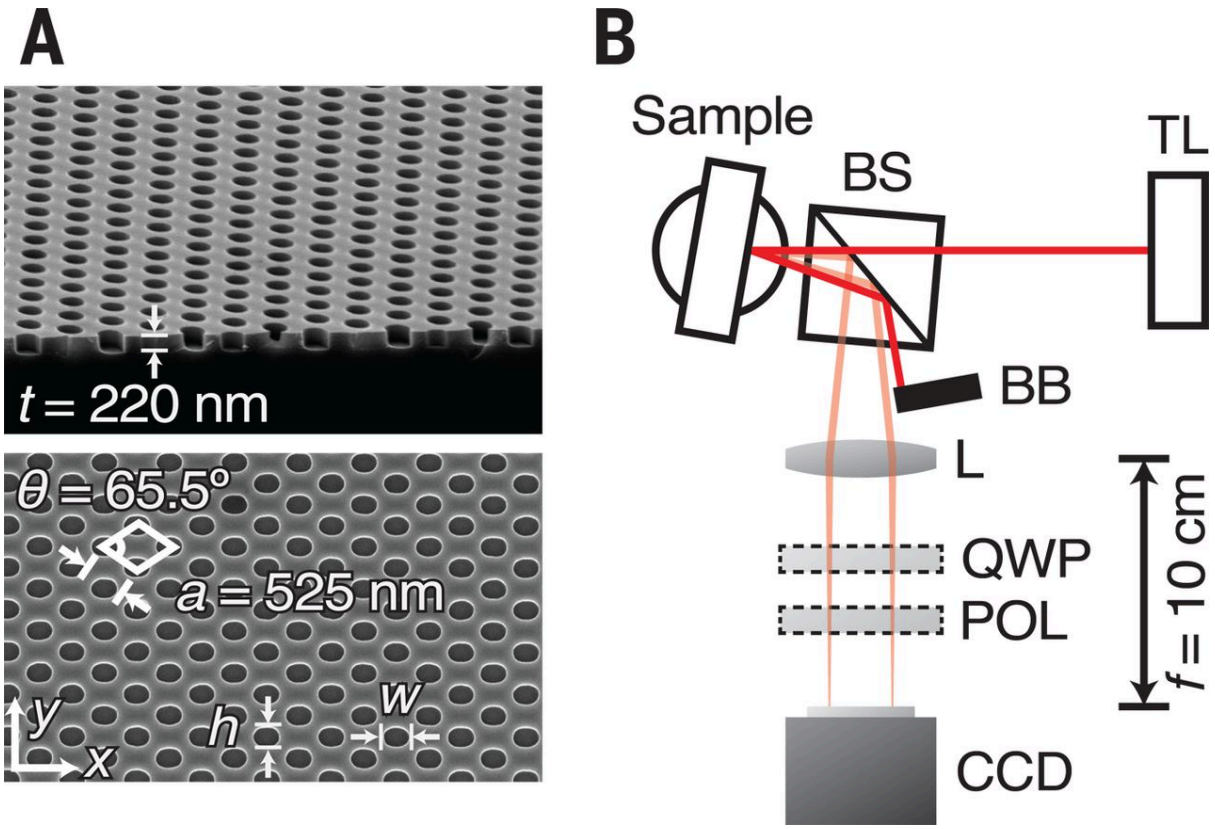

Fig. 2 Fabricated PhC slab and measurement setup. (**A**) SEM images of the PhC samples: side view (top panel) and top view (bottom panel). (**B**) Schematic of the scattering measurement setup. Vertically polarized light from a tunable continuous-wave Ti-Sapphire laser (TL) scatters off the PhC slab and is collected by a CCD camera placed at the focal plane of the lens (L). The specular reflection is blocked to ensure only scattered light is imaged. POL and QWP are used in polarimetry measurements of the scattered light. TL, tunable laser; BS, beam splitter; L, convex lens with 10-cm focal length; QWP, quarter-wave plate; POL, polarizer; BB, beam block.

We performed angle-resolved scattering measurements (setup shown above) to image isofrequency contours of the sample. The PhC sample is illuminated with a tunable continuous-wave Ti:Sapphire laser that is vertically polarized, while scattered light—arising from natural fabrication imperfections of the sample—is collected with a charge-coupled device (CCD) camera placed at the focal plane of a convex lens with -cm focal length. Because of resonant enhancement, the scattered light will have strongest intensity only along directions where the underlying resonances share the same frequency as the pump laser, and thus the isofrequency contours of the sample are directly imaged onto the CCD. Compared to previous measurement

techniques based on the reflection spectrum, this scattering method enables fast and direct extraction of band information, without fitting to any specific models. To show the full shrinking-and-reexpanding feature of the isofrequency contours around the bulk Fermi arc, the laser wavelength is tuned from 794 nm down to 788 nm at steps of ~0.2 nm. Furthermore, the polarization at each point along a given isofrequency contour is determined through polarimetry measurements, by optionally inserting a quarter-wave plate and a polarizer in front of the CCD .

At a few representative wavelengths around the Fermi arc, the numerical results of isofrequency contours obtained from simulating extracted structural parameters are plotted against the experimental results , showing good agreement with each other. Here, for better comparison, the numerical results are offset by 0.5 nm relative to the experiments. To focus on the bulk Fermi arc, we highlight the region of interest in both panels, where the isofrequency contours clearly demonstrate the shrinking and re-expanding behavior. As shown below, as the wavelength decreases from 794.0 nm, the corresponding isofrequency contour shrinks (top two rows), and eventually becomes an open-ended arc at 791.0 nm (middle row), consistent with our previous theoretical predictions. As the wavelength is further decreased down to 789.5 nm and 788.7 nm, the arc expands out into closed contours again (bottom two rows). The bending feature of the contours is a result of higher-order terms in the band dispersion. The open contour at 791.0 nm (middle row) is a clear, direct observation of the bulk Fermi arc.

So far, we have shown one direct consequence of the unique double–Riemann sheet topology near paired EPs—the bulk Fermi arc. Next, we demonstrate another consequence: half-integer topological charges in the polarization configuration, which also serve as a direct experimental proof of the topological index of an EP. These topological charges describe the direction (clockwise or counterclockwise) and number of times the polarization vector winds around a point or line singularity in the optical field, and in our particular system, we observe a robust 180° winding around the Fermi arc, corresponding to a half-integer topological charge. To fully reconstruct the far-field polarization configurations of the resonances, we perform polarimetry measurements by recording the intensity of isofrequency contours after passing through six different configurations of polarizers and/or waveplates. Although the incoming light is vertically polarized, the scattered light at each point along the contour is, in general, elliptically polarized, reflecting the polarization state of its underlying resonance. Taking points X and Z as examples: After passing through a vertical polarizer, the scattered light is weak (strong) at point X(Z); whereas after a horizontal polarizer, the relative intensity of the scattered light switches between points X and Z. This clearly shows that the far field of the underlying resonance at point X(Z) is mostly horizontally (vertically) polarized.

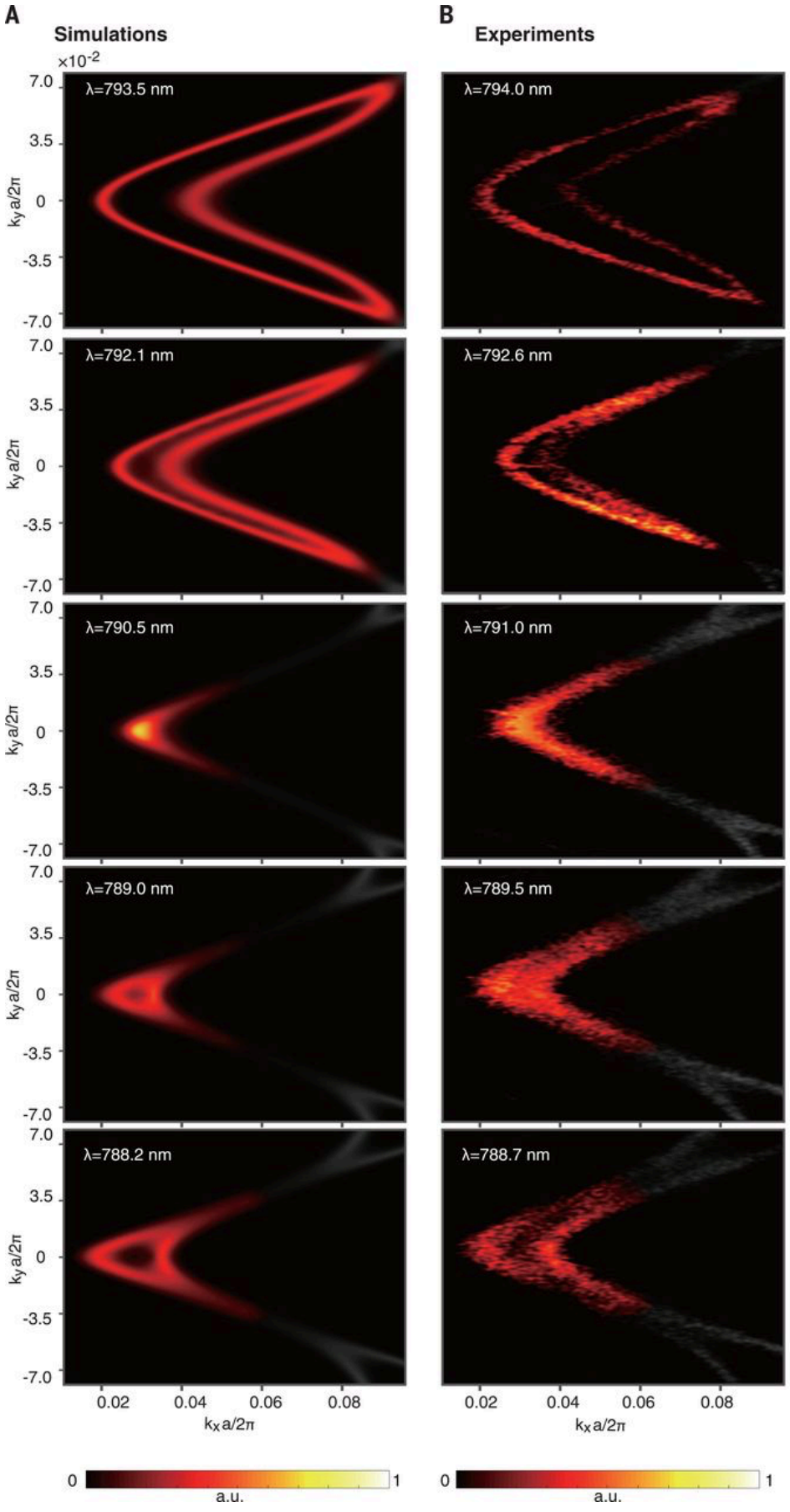

Fig. 3 Experimental demonstration of a bulk Fermi arc. (**A**) Numerically simulated spectral density of states and (**B**) experimentally measured isofrequency contours at five representative wavelengths. The bulk Fermi arc appears at 791.0 nm (middle row), when the isofrequency contour becomes open-ended. The regions of interest are highlighted in all panels to emphasize the shrinking (top two rows) and reexpanding (bottom two rows) feature of isofrequency contours near the bulk Fermi arc. The numerical results are offset by 0.5 nm for better comparison.

We have demonstrated that the topological properties of paired EPs endow the band structure and far-field emission with unique features, manifested as the emergence of bulk Fermi arcs and polarization half topological charges. Our structure also provides an easily realizable method to create half-integer vector-vortex beams at a wide range of frequencies. Future prospects leveraging the topological landscape around paired EPs may enable PhC lasers with exotic emission profiles, such as twisted Möbius strips. The isolated EPs found in our structure also provide a straightforward platform for studying the influence of EPs and their topology on light-matter interactions, such as modified Purcell factors for spontaneous emission enhancement and nonlinear optics generation. Our observation of bulk Fermi arcs and polarization half charges extends the existing framework of topological physics in closed systems into a new regime involving open systems and provides a platform for the future exploration of non-Hermitian topological physics in general wave systems, ranging from photonic and acoustic to electronic and polaritonic systems.

2. Exceptional surfaces in PT symmetric non-Hermitian photonic systems (Optica 6, 2, 2019)

Exceptional points in non-Hermitian systems have recently been shown to possess nontrivial topological properties and to give rise to many exotic physical phenomena. However, most studies thus far have focused on isolated exceptional points or one-dimensional lines of exceptional points. Here, we substantially expand the space of exceptional systems by designing two-dimensional surfaces of exceptional points, and find that symmetries are a key element to protect such exceptional surfaces. We construct them using symmetry-preserving non-Hermitian deformations of topological nodal lines, and analyze the associated symmetry, topology, and physical consequences. As a potential realization, we simulate a parity-time-symmetric 3D photonic crystal and indeed find the emergence of exceptional surfaces. Our work paves the way for future explorations of systems of exceptional points in higher dimensions, and applications in emission control and sensing.

In recent years, there has been growing interest in exploring novel effects in non-Hermitian systems. This has provided great insight in fundamental science, including parity-time PT symmetry and novel topological phases, while also opening the doors to new photonic applications, such as unconventional transmission and reflection, sensing functionalities, lasers, and chiral mode transfer. Key to many of these explorations are the special properties of exceptional points (EPs)—unique spectral degeneracies where the real and imaginary parts of two or more

eigenvalues coincide and the eigenvectors coalesce. Indeed, only realizable in non-Hermitian systems, EPs mark the boundaries of PT phase transitions and give rise to the unconventional optical responses mentioned above. Moreover, they possess topological properties such as a Berry phase and vorticity, and can give rise to open Fermi arcs in the bulk dispersion of systems. However, the majority of studies thus far have focused on the properties of isolated points (0D) or continuous lines (1D) of EPs. Correspondingly, this has limited the types of achievable band dispersions and observable phenomena in these non-Hermitian systems. This calls for approaches to go beyond these lower-dimensional EP systems and explore higher-dimensional configurations, such as surfaces of EPs.

Here, we propose and analyze several models to realize exceptional surfaces. First, we examine the general conditions for EPs to occur, and find that the emergence of EP surfaces requires additional symmetry protection, indicating that EP surfaces can be understood as the generalization of Hermitian symmetry-protected nodal phases to the non-Hermitian setting. Motivated by this, we consider a non-Hermitian deformation of topological nodal lines, and show that under certain symmetry conditions, this can give rise to a non-Hermitian system with EPs configured in a torus geometry. We show that the EP torus is characterized by separated components inside and outside the torus, as well as a quantized non-Hermitian Berry phase inherited from the Hermitian nodal line. In addition, we find that the EP surface encloses an open nodal volume—a three-dimensional generalization of bulk Fermi arcs—in which the real parts of two bands are degenerate with each other within an entire volume. This offers remarkable control of the band structure and spectral density of states (DOS) of the system, which could have interesting applications such as controlling spontaneous emission and enhancing nonlinearities in optical systems. Finally, we utilize PT-symmetric gain-loss modulation in a simple three-dimensional photonic crystal structure to realize EP surfaces, which can be readily implemented in experiments. Our results are of particular interest to the photonics community, where non-Hermitian terms are often naturally present in the form of gain, material loss, or radiation loss.

We start by considering the conditions to create EPs, in order to understand why 0D or 1D EP configurations are typically generated. EPs occur when the real and imaginary parts of two or more eigenvalues coalesce and the eigenspace becomes defective.Thus, we shall generically find that two constraints need to be satisfied to create an EP. The dimensionality of the EP contour generated will then be $d-2$ in spatial dimension d, as observed in previous experiments. However, this also implies that additional mechanisms are required to realize EP surfaces in physical dimensions within 3. At this stage, it is instructive to examine the case of Hermitian systems: in 3D, the robust spectral degeneracies are 0D Weyl points, and the realization of 1D nodal lines requires symmetry protection. In analogy, we also expect the 2D EP surfaces to be symmetry-protected and serve as a natural non-Hermitian generalization of symmetry-protected topological nodal phases. The

symmetry conditions, which can include crystalline symmetries or more general non-Hermitian symmetries, can reduce the number of independent equations that need to be simultaneously satisfied, leading to a $d-1$ dimensional EP configuration in d dimensions. In analogy to lower-dimensional examples, we expect $\mathscr{PT}$ symmetry to be one such symmetry sufficient to generate EP surfaces in 3D. We note that adding a constant gain/loss term will not change the spectral degeneracies, and thus the system will still host EP surfaces

Motivated by the fact that both Hermitian nodal lines and EP surfaces can be protected by PT symmetry, we now consider symmetry-preserving non-Hermitian deformations to Hermitian nodal lines. This approach thus directly makes clear the connection between EP surfaces—examples of non-Hermitian nodal phases—and their Hermitian counterparts. Compared with previous work that has studied non-Hermitian nodal lines, the symmetry preservation plays a key role in generating EP surfaces as opposed to lines of EPs.

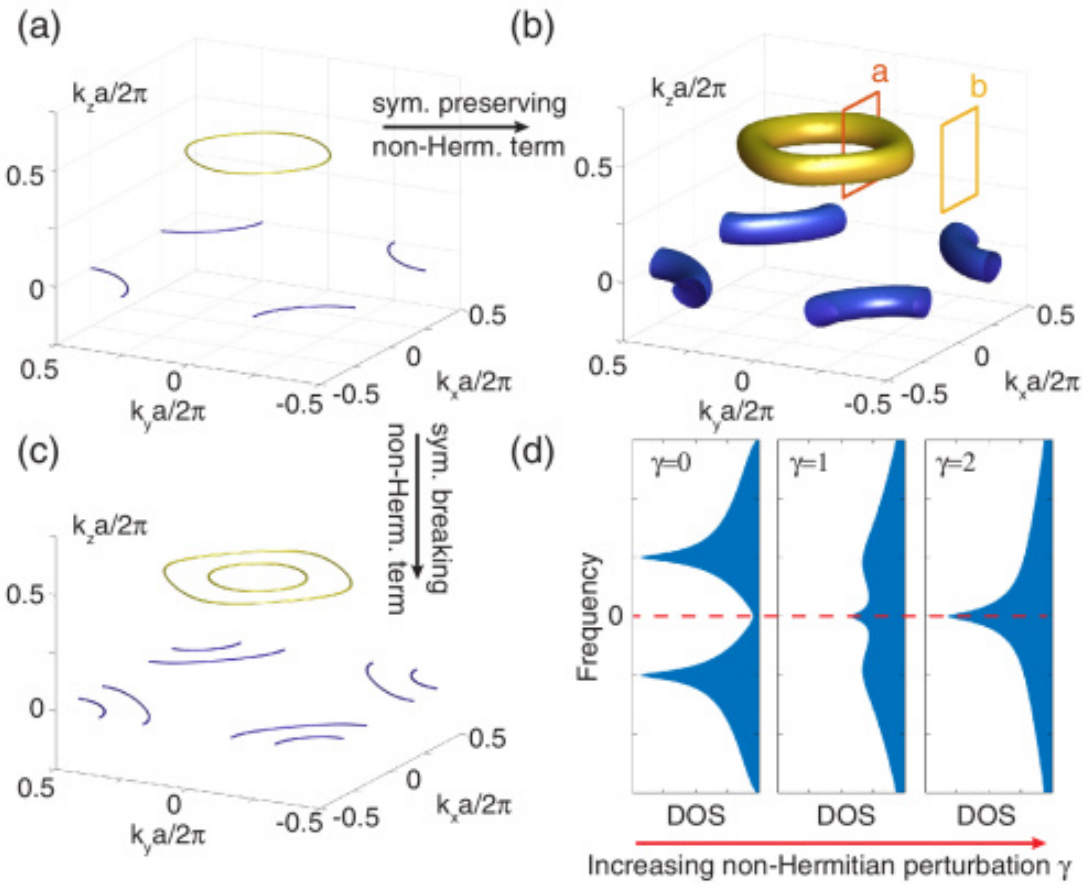

Fig. 4. (a)–(c) Spectral degeneracies in Hermitian and non-Hermitian systems. The Hermitian nodal line (a) is protected by PT symmetry. A symmetry-preserving non-Hermitian perturbation produces an exceptional torus (b), whereas a symmetry-breaking one produces exceptional rings (c). (d) Spectral DOS for increasing non-Hermitian perturbation γ, with the DOS close to the nodal line frequency (red dashed line) increasing significantly.

The physics discussed here can be easily realized in microwave experiments consisting of a metallic-mesh 3D photonic crystal. Nodal chains have been discovered in this simple structure, where the nodal lines are protected by PT symmetry and the chain crossing point is additionally protected by a mirror symmetry. By adding non-Hermitian perturbations that preserve the PT symmetry, as shown in Fig. 2(a), each nodal line can be split into an EP surface. The deformation to the chain crossing point, however, can be more complicated, and in general may lead to novel EP geometries. Although the presence of symmetry-breaking terms will gap out the nodal chain crossing point, a non-Hermitian term that is larger in magnitude can restore the connectedness of the feature, even if the mirror symmetry of the system is broken.

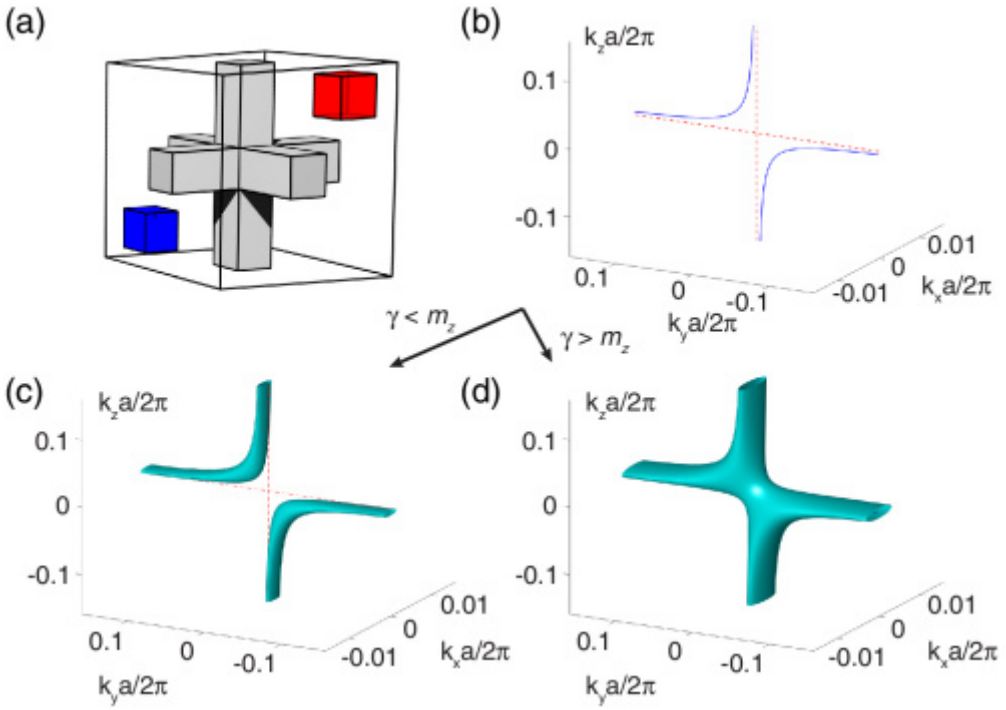

Fig. 5. (a) Unit cell of a periodic metallic mesh structure with $\mathscr{PT}$-symmetric perturbation to realize a nodal chain in the Hermitian limit and an EP surface under non-Hermitian perturbations. (b) The nodal chain crossing point (red dashed lines) can be gapped out by a mass term (blue solid lines). Depending on the non-Hermitian perturbation strength, the gap between the EP tori can remain (c) or they can become connected (d).

We now analyze the topological properties associated with the EP torus. For a Hamiltonian with PT symmetry, we can choose a basis such that the PT symmetry corresponds to complex-conjugation, in which case the Hamiltonian must be real, and complex eigenvalues come in complex-conjugate pairs. Therefore, when changing a Hamiltonian in which all eigenvalues are real into one with complex-conjugate pairs, the continuity of eigenvalues requires a degeneracy of eigenvalues on the real line to appear in between, corresponding to an EP. Thus, the inside (complex eigenvalues) and outside (real eigenvalues) of the torus belong to two disconnected branches, and there must exist a continuous surface of EPs in

between them. In addition, we find that the generalization of the Hermitian Berry phase protects the EP surface to form a continuous torus. For the preceding models, we calculate the Berry phase along different paths outside the torus using the normalized eigenvectors. For a path not linking with the EP torus [Fig. 4(b), path b], the Berry phase is 0; whereas, along a path linking with the EP torus [Fig. 4(b), path a], we find that the Berry phase is π. This is consistent with the π Berry phase for the Hermitian nodal line, indicating that the topological invariant is inherited by the non-Hermitian system, and the topological protection against the EP torus breaking apart remains.

The generation of EP surfaces also has important consequences for the bulk dispersion. Similar to the bulk Fermi arcs that terminate at discrete EPs, the internal volume of the EP surface will have a pair of bands that are completely degenerate in the real part of their eigenvalues, which we call an open nodal volume. The non-Hermitian term then provides remarkable control of the spectral DOS of the system: as we continuously increase the non-Hermitian perturbation from 0 to a large value, the DOS near the nodal line frequency will be tuned from a relatively small value, due to the 1D nature of the nodal line, to a large value, due to the 3D volumetric factor of the open nodal volume. We calculate the spectral DOS for the model Eq. (2), incorporating the linewidth as a Lorentzian broadening, such that the calculated values are directly relevant to physical consequences such as spontaneous emission enhancement. In view of experiments, we have added a constant loss term $\gamma 0=\gamma+0.1$ to make the system passive. The results are illustrated in Fig. 4(d), where the spectral DOS near the nodal line clearly increases as the strength of the non-Hermitian perturbation is increased.

In physical realizations of nodal lines and the corresponding EP surfaces, a nodal line may not be completely flat in frequency, which will cause some reduction of the accessible range of DOS. However, the structure shown in Fig. 5(a) has been shown to have a remarkably uniform nodal line frequency in the Hermitian limit, with less than 1% variations across the whole Brillouin zone. This makes it a promising system to observe the EP torus discussed here, as well as to investigate the evolution of DOS with the strength of the non-Hermitian term. In addition, the system can be engineered to possess a non-Hermitian particle-hole symmetry, which can protect the nodal volume to be completely flat. The continuous controllability of DOS via non-Hermitian modulation may enable spontaneous emission engineering, while the higher dimension of the EP surface may lead to interesting opportunities in sensing. The EP surface also enables a PT-superprism effect, in which small changes in incident wave angle can dramatically change the gain/loss response.

In this work, we have proposed various methods to realize EP surfaces; analyzed their symmetry, topology, and applications; and discussed straightforward avenues to their experimental implementation in photonic and microwave systems. We have also shown that the bulk dispersion of these systems is drastically modified by including symmetry-preserving non-Hermitian terms, giving rise to a highly

tunable DOS. While we have focused on systems with PT symmetry, the analysis can be readily generalized to other types of symmetries, including general non-Hermitian symmetry classes and crystalline symmetries. Similarly, it may be interesting to consider other types of invariants, particularly those unique to non-Hermitian systems. In addition, one could study the associated bulk-boundary correspondence, where unusual phenomena such as the non-Hermitian skin effect emerge.

3. Floquet Chern insulators of light (Nature Communications 10, 4194, 2019)

Achieving topologically-protected robust transport in optical systems has recently been of great interest. Most studied topological photonic structures can be understood by solving the eigenvalue problem of Maxwell's equations for static linear systems. Here, we extend topological phases into dynamically driven systems and achieve a Floquet Chern insulator of light in nonlinear photonic crystals (PhCs). Specifically, we start by presenting the Floquet eigenvalue problem in driven two-dimensional PhCs. We then define topological invariant associated with Floquet bands, and show that topological band gaps with non-zero Chern number can be opened by breaking time-reversal symmetry through the driving field. Finally, we numerically demonstrate the existence of chiral edge states at the interfaces between a Floquet Chern insulator and normal insulators, where the transport is non-reciprocal and uni-directional. Our work paves the way to further exploring topological phases in driven optical systems and their optoelectronic applications.

Here, we study Floquet topological phases in general nonlinear PhCs under external drive and show how non-reciprocal transport can be achieved in a Floquet Chern insulator. We start by formulating the Floquet eigenvalue problem of Maxwell's equations, and show it is necessarily non-Hermitian but with real eigenvalues in many cases. After elucidating what time-reversal symmetry (T) entails in driven systems, we engineer the external drive to break T and to close and re-open Floquet gaps to change bands Chern numbers. Finally, through numerical simulations of realistic designs, we present an explicit example of a Floquet Chern insulator, along with the dispersions and locations of uni-directional chiral edge states at its interfaces with normal insulators.

We start by showing that new bandgaps—Floquet gaps—can be created in driven nonlinear PhCs, which do not exist in the static band structure. We consider a two-dimensional PhC that involves second-order optical nonlinear materials such as LiNbO3. The static band structure is schematically shown in Fig. 6b, and we focus on two isolated bands: $|1\rangle$ in blue and $|2\rangle$ in red, which are separated by a gap in the spectrum. When an external driving field at frequency Ω is applied along the normal direction, the discrete spatial translation symmetry of the system is preserved, but the continuous temporal translation symmetry is broken, leaving only a discrete temporal translation symmetry. Accordingly, each band creates copies of

itself—Floquet bands—shifted up or down in the spectrum by $m\Omega$, where m is an integer. When Ω is slightly larger than the static gap, two of the Floquet bands, $|1, m = 0\rangle$ and $|2, m = -1\rangle$, cross, and the coupling between them $V21$ opens a new gap—Floquet gap—that is controlled by the driving field. When the driving field is weak, the size of the Floquet gap is linearly proportional to the coupling strength $|V21|$, meaning this gap can only be closed at momentum (k) points where the complex coupling term vanishes: $V21(k) = 0$. We later show these singular points represent the topological phase transitions between Floquet Chern insulators and normal insulators.

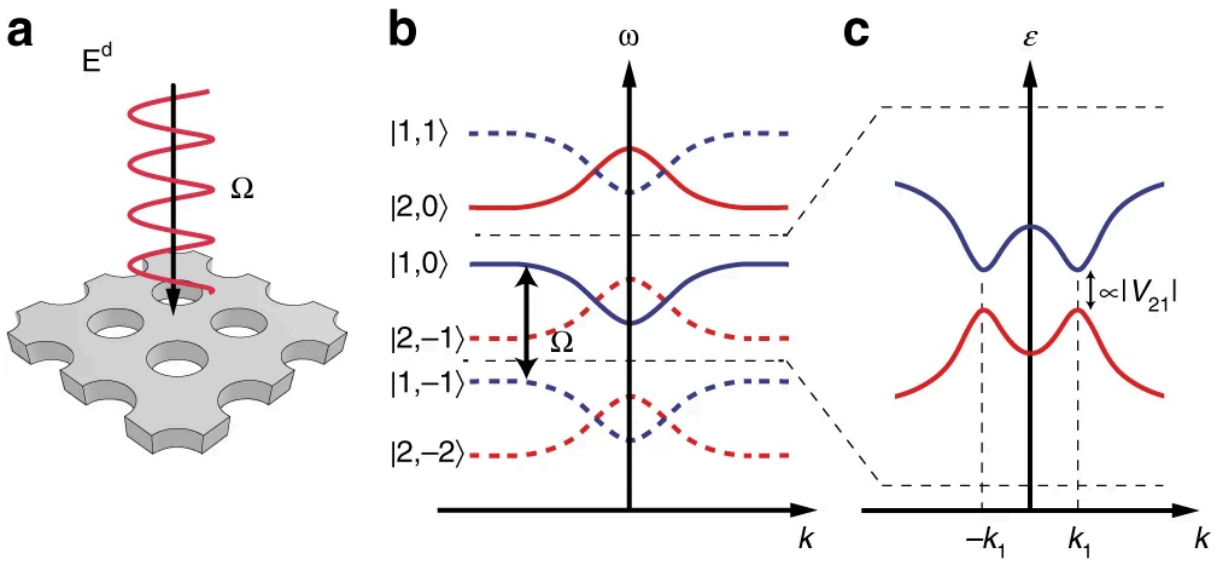

Fig. 6 Floquet bands and gaps in a periodically driven nonlinear photonic crystal. a Schematic of a nonlinear photonic crystal (PhC) placed in a monochromatic driving field Ed at frequency Ω. b Due to the periodic drive, static bands of the PhC (solid lines) create copies of themselves—Floquet bands (dashed lines)—by shifting up or down in the spectrum. c Two of the Floquet bands $|1, m = 0\rangle$ and $|2, m = -1\rangle$ cross at $\pm k1$. Their coupling term $V21$ opens a new gap Eg—Floquet gap—and its size is linearly proportional to the magnitude of their coupling strength $|V21|$ under weak drive

To better illustrate some of the key concepts, we focus on an example when two bands become close to each other under driving $\omega 2 - \omega 1 \approx \Omega$, while both are far away from other bands. Hence, we restrict the trial solutions to the subspace spanned by the two bands for simplicity; however, the presented formalism is general and not limited to the two-band model. Under a further rotating-wave approximation, the Floquet eigenvalue problem can be simplified into. As shown, this generalized eigenvalue problem is indeed non-Hermitian, but its eigenvalues can be guaranteed as real under some conditions. For example, when the driving field is exactly on-resonance, namely $\omega 2 = \omega 1 + \Omega$, the two Floquet eigenvalues can be further simplified as: . The normalized gap size is linearly proportional to $|V21|$, whose magnitude is determined by both the modal overlap and the driving field

strength. Furthermore, we note that both eigenvalues are necessarily real as long as we are coupling bands both at positive (or negative) frequencies ($\omega 1 \omega 2 > 0$). Physically, these scenarios are analogous to the depletable sum-frequency generation: power oscillates between a depletable pump $\omega 1$ and the sum-frequency beam $\omega 2$, but their total photon number remains fixed in time. On the other hand, complex eigenvalues may appear when a positive-frequency mode is coupled to a negative-frequency mode ($\omega 1 \omega 2 < 0$) and the resulting Floquet modes may grow exponentially in time. These scenarios are analogous to optical parametric amplification where a non-depletable pump beam ($|\omega 1| + |\omega 2|$) amplifies the signal and idler beams. Here, we focus on the first situation where Floquet eigenvalues are real. Topological phase transitions can only happen at k points where the gap is closed, requiring the coupling term $V21 = 0$. This is equivalent to requiring the complex phase $\arg V21$ to be undefined, or to be a topological defect, in k space. The topological phase transitions, being topological defects, are thus robust against any perturbations that modify the complex coupling terms $V21$, as such perturbations cannot get rid of the topological phase transitions but shift their positions in the 3D parameter space of (kx, ky, Ω).

Next, we show how such topological defects can be synthesized by engineering the polarization of the driving field. Our considered PhC sample is shown in Fig. 7, which is consisted of a hexagonal lattice, with lattice constant a, of regions made of silicon () and regions made of z-cut LiNbO3. Both inversion and rotation symmetries are broken to lift all degeneracies at high-symmetry k points. The static band structure is calculated using Finite Element Methods (see Methods section for details) and shown in Fig. 7. In the static structure, TE bands (Hz, Ex, Ey; red) are decoupled from the TM bands (Ez, Hx, Hy; blue), due to the mirror symmetry in the z direction. However, under a driving field polarized in the xy plane, TE and TM bands are coupled: specifically, the external field drives the second-order optical nonlinearity of LiNbO3, and , and creates and terms in the effective permittivity tensor of LiNbO3. These four terms break the mirror symmetry in z and couple the Ez component of a TM mode to the Ex,y components of a TE mode. By analyzing the nonlinear optical property of LiNbO3, one can show only TE-TM bands are coupled via modulation in this setup, while the Floquet TE-TE or TM-TM bands will not couple to each other. We found that time-reversal symmetry (T) in the Floquet eigenvalue problem is defined as . Furthermore, we found T is preserved when the driving field is linearly polarized and no topological Floquet gap can be opened. On the other hand, elliptically polarized driving fields break T. The condition on T in these two scenarios can be intuitively understood by analyzing the temporal evolution of the instantaneous optical principle axes of LiNbO3: under a linearly polarized monochromatic drive, one optical axis remains static, while the other two oscillate in a time-reversal symmetric manner. In comparison, under an elliptically polarized drive, all three optical axes rotate around the z axis at the driving frequency and this spinning behavior breaks T.

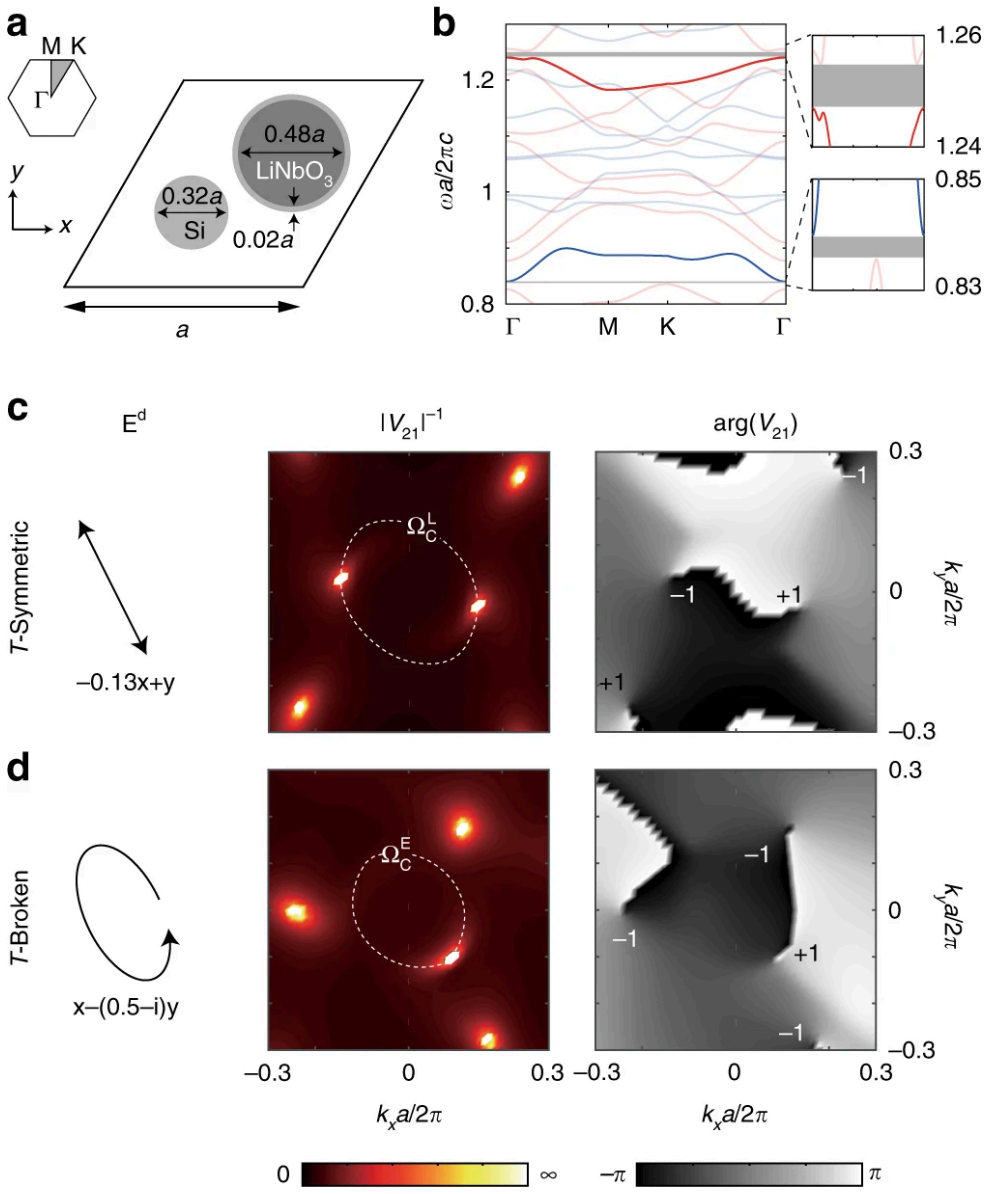

Fig. 7 Topological charges in modal coupling terms and the influence of time-reversal symmetry. a Nonlinear PhC unit cell involving Si and *z*-cut LiNbO3. The centers of the Si and LiNbO3 rods are at () and () with respect to the bottom-left corner of the unit cell. b Static modes are separated into TE (red) and TM (blue) bands. Under a driving field polarized in the *xy* plane, a TE band is coupled to a TM band through $\chi(2)$ of LiNbO3. Their coupling term $V21$ is controlled by the polarization of the drive. c Under a linearly polarized drive (), pairs of vortices with opposite topological charges (±1) are found in the complex phase arg$V21$, located at opposite k points. At these k points, the modal coupling term vanishes and $1/|V21| \rightarrow \infty$. d Under an elliptically polarized drive, , vortices in arg$V21$ appear without any symmetry. Topological phase transition is achieved between a Floquet normal insulator and a Floquet Chern insulator through a single topological charge at (dashed circle)

The properties associated with time-reversal symmetry are confirmed in our simulation results of the modal coupling terms $V21$ as shown in Fig. 7. Specifically, under a linearly polarized drive (T-symmetric), $V21$ reduces to 0 at pairs of opposite k points that are related by T-symmetry, shown as bright spots in Fig. 7c. Furthermore, each pair of topological defects carry opposite topological charges q, which are defined through the winding numbers of the complex phase. Here C is a closed path in k space that encircles the defect in the counter-clockwise direction. Consequently, the Floquet gap can be closed and re-opened by tuning the driving frequency through a critical value (dashed circle); however, the transitions always happen at a pair of opposite k points and the Floquet bands are always topologically trivial. See Supplementary Note 6 for the definition of Berry curvature and Chern number of Floquet bands. On the other hand, under an elliptically polarized drive (T-broken), topological defects appear without any symmetry (Fig. 7). As a result, the Floquet gap can close and re-open at a single k point, as $V21(k)$ is no longer related to $V21(-k)$. In our system, this topological phase transition happens at another critical value (dashed circle).

Next, we study topological phase transitions between Floquet Chern insulators and normal insulators and show these transition points are singular points in the parameter space of (kx, ky, Ω) as shown in Fig. 8a. First, the Floquet band gap closes at the transition point, but grows linearly as Ω deviates from Ω2 (Fig. 8b). Furthermore, we compare the Floquet spectra near the transition point: the bands are gapped when either $\Omega > \Omega 2$ (left panel of Fig. 8d) or $\Omega < \Omega 2$(right); however, the two Floquet bands touch at a singular point in k space in a linear fashion when $\Omega = \Omega 2$ (middle). We note the small difference between Ω2 and arises from the difference between full Floquet formulation we adopt here and results under rotating-wave approximation. The gap size grows linearly as the system parameter deviates from a single point in the three-dimensional parameter space of (kx, ky, Ω), therefore, the transition points can also be interpreted as synthetic Weyl points. We further track the Chern numbers of the Floquet bands as Ω is varied: the Chern number of the top (bottom) band changes by −1 (1) as the modulation frequency reduced from $\Omega 1a/2\pi c = 0.395$ (Floquet normal insulator) to $\Omega 3a/2\pi c = 0.37$ (Floquet Chern insulator), through $\Omega 2a/2\pi c = 0.383$ (Fig. 9c). In addition, the Chern numbers of the two bands jump in opposite directions with their sum fixed at 0, which confirms our system is a Chern insulator. Similarly, the Floquet gap can also be closed and re-opened under linearly polarized driving fields. For example, by tuning Ω through a critical value of , the Floquet gap is closed and re-opened, but at a pair of opposite k points. Through this process, all bands remain topologically trivial with zero Chern numbers due to the presence of T-symmetry.

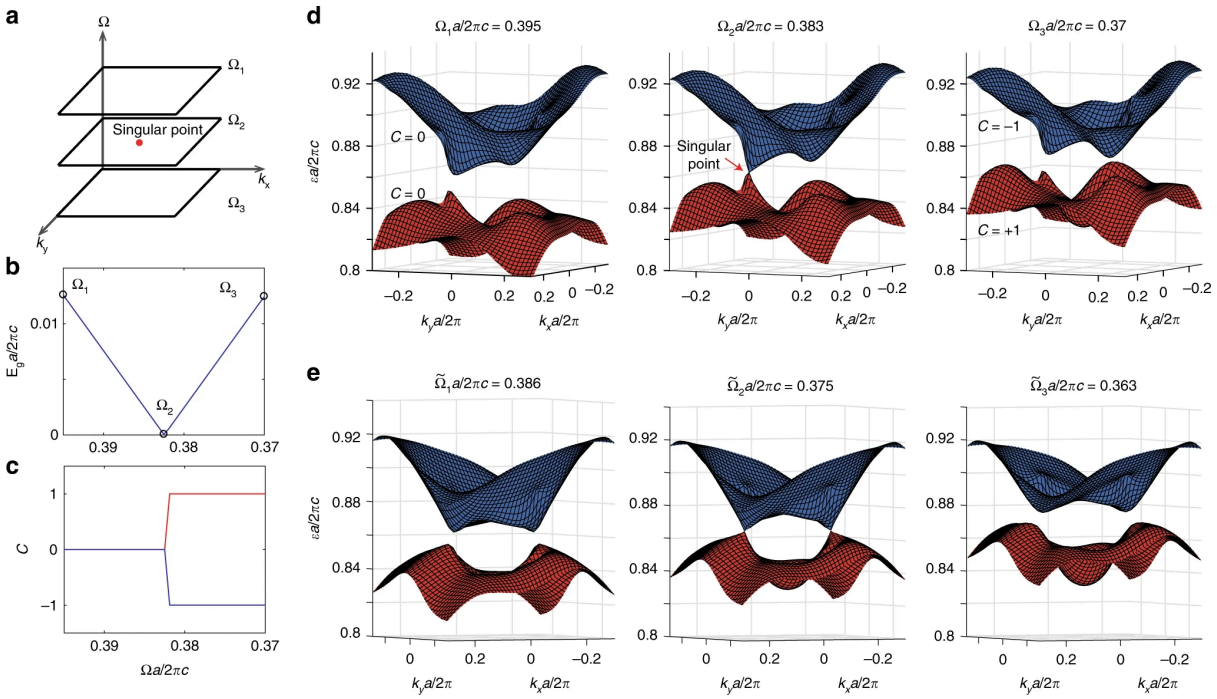

Fig. 8 Topological phase transition points in 3D synthetic parameter space. a The topological phase transition point is defined in the parameter space of (*kx*, *ky*, Ω). b Under an elliptically polarized drive, the Floquet band gap closes at $\Omega 2a/2\pi c = 0.383$, and increases linearly in its vicinity on both sides. Here we plot the partial gap size defined as the minimum of partial gap in the k space. c Under an elliptically polarized drive, the Chern numbers of the top (blue) and bottom band (red) change by 1 as Ω scans through Ω2. d The Floquet band structure shows a linear touching between the top and bottom bands at a singular k point at Ω2 (middle panel). This singular point represents a topological phase transition between a Floquet normal insulator (Ω1, left) and a Floquet Chern insulator (Ω3, right). e In contrast, the Floquet band gap closes and re-opens at a pair of opposite k points for *T*-symmetric drive when tuning driving frequency from to and is thus topologically trivial

Finally, we show the existence of chiral edge states at the interfaces between a Floquet Chern insulator (gray region in Fig. 10a) and normal insulators (white region). In this super-cell geometry, we apply periodic boundary conditions in both *x* and *y* directions, and these two insulators have two interfaces, top and bottom. The topological region shares the same setup as the right panel of Fig. 9d; the trivial region is driven at the same frequency $\Omega 3a/2\pi c = 0.37$, but with a linearly polarized light that preserves *T*. Through a super-cell calculation, all bands in the system are computed. Aside from the bulk bands in the trivial and nontrivial regions, we see chiral edge states (red and blue lines) emerge at the two interfaces with frequencies going across the topological band gap. Their mode profiles further confirm these are indeed edge states localized at the top (red) and bottom (blue) interfaces (Fig. 9c); in comparison, a bulk mode (black) is delocalized along the *y*-direction. As a control experiment, when the driving frequency is changed to Ω1 such that all regions are

topologically trivial, no gapless chiral edge state is observed in such scenario (Fig. 9d). This confirms the number of chiral edge states and their traveling directions are consistent with the Floquet topological band theory results for electronic systems. We note that the photon number is conserved in edge state transport. This is to be distinguished from a previous study using nonlinear parametric driving by Peano et al.[33], where the photon number is not conserved, and the edge state transport becomes inelastic. Although helical spatial modulation of waveguide arrays achieves Floquet Chern insulators in the transverse plane, our approach breaks reciprocity for the system as a whole and thus enables optical isolation through the chiral edge states.

To sum up, we present a general framework to achieve Floquet topological phases in nonlinear photonic crystals, defined by the Floquet eigenvalue problems in Maxwell's equations. We show that Floquet band gaps can be closed and re-opened in a virtually arbitrary fashion by engineering the driving field (polarization and frequency). Using this framework, we propose and numerically demonstrate a Floquet Chern insulator of light by breaking time-reversal symmetry using elliptically polarized driving fields. We show the Floquet topological phase transitions are through singular points of modal coupling terms in 3D parameter space. Finally, we numerically demonstrate the existence of chiral edge states at the interfaces between topologically trivial and non-trivial regions. Our work paves the way to further classifying and realizing topological phases in dynamically driven optical systems and their optoelectronic applications in communication and signal routing. Our method of inducing Floquet topological phases is also applicable to other wave systems, such as phonons, excitons, and polaritons.

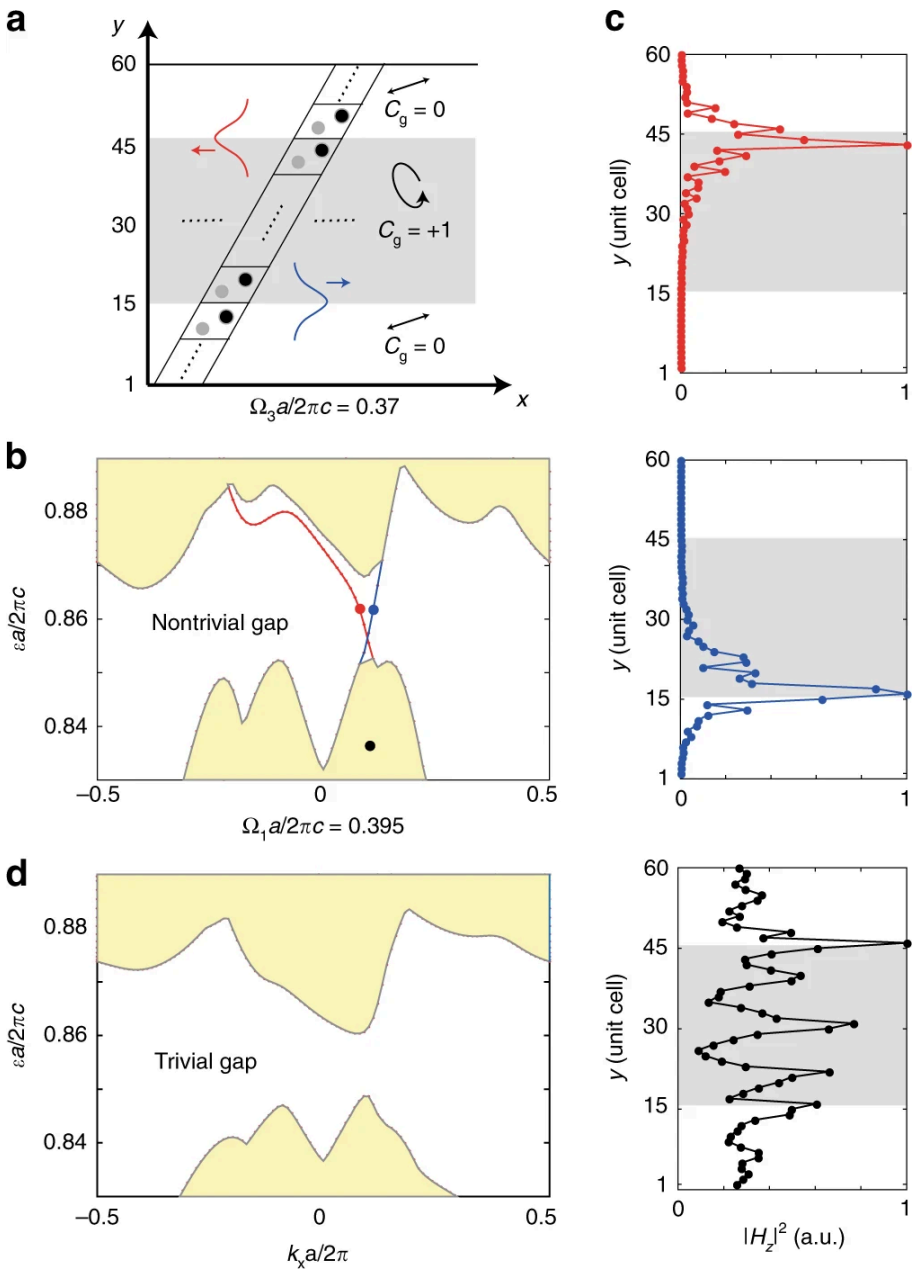

Fig. 9 Characterizations of chiral edge states at the interfaces between a Floquet Chern insulator and normal insulators. a Schematic of the super-cell geometry with a Floquet Chern insulator placed in between two Floquet normal insulators. The Floquet Chern insulator is the same setup as the right panel of Fig. 7. All regions are driven at the same frequency Ω3, and the associated gap Chern number for the Floquet insulator is *C*g = 1. b The dispersion along *kx* axis shows two types of modes: bulk bands in the normal and Chern insulator regions (yellow) and uni-directional chiral edge states at the top and bottom interfaces (red and blue). c Chiral edge states are absent in the projected dispersion when all regions are driven at frequency Ω1 before the topological phase transition. d Comparison among the mode profiles of a bulk state (black), the chiral edge states localized at the top interface traveling to the left (red) and at the bottom interface traveling to the right (blue).

4. Topologically enabled ultrahigh-Q guided resonances robust to out-of-plane scattering (Nature 574, 501, 2019)

To sum up, we present a general framework to achieve Floquet topological phases in nonlinear photonic crystals, defined by the Floquet eigenvalue problems in Maxwell's equations. We show that Floquet band gaps can be closed and re-opened in a virtually arbitrary fashion by engineering the driving field (polarization and frequency). Using this framework, we propose and numerically demonstrate a Floquet Chern insulator of light by breaking time-reversal symmetry using elliptically polarized driving fields. We show the Floquet topological phase transitions are through singular points of modal coupling terms in 3D parameter space. Finally, we numerically demonstrate the existence of chiral edge states at the interfaces between topologically trivial and non-trivial regions. Our work paves the way to further classifying and realizing topological phases in dynamically driven optical systems and their optoelectronic applications in communication and signal routing. Our method of inducing Floquet topological phases is also applicable to other wave systems, such as phonons, excitons, and polaritons.

Here we theoretically propose and experimentally demonstrate on-chip photonic resonances that are much less susceptible to out-of-plane-scattering losses than expected, owing to their unique topological features. We start by showing that resonances with ultrahigh Q can be achieved by merging multiple BICs. First, we consider a photonic crystal slab (Fig. 10a), in which a square lattice (periodicity a = 519.25 nm) of circular air holes (radius r = 175 nm) is patterned in silicon (thickness h = 600 nm). With the use of numerical simulations (using the COMSOL Multiphysics software), we focus on the transverse electric (TE) A band (red line), featuring nine BICs where Q diverges to infinity (Fig. 10b). The topological nature of the BICs can be understood from the corresponding far-field polarization plots (Fig. 10b, bottom panels), where each BIC appears as a topological defect (vortex) in the polarization long axes characterized by an integer topological charge of ±1. Among these nine vortices, one is pinned at the centre of the Brillouin zone owing to symmetry, whereas the locations of the remaining eight can be controlled by varying system parameters such as the periodicity. For example, when a increases from 519.25 nm to 531.42 nm, the eight off-centre BICs move towards the centre until all nine of them merge into a single BIC with a charge of +1 when a = 531.42 nm. This single BIC persists when a further increases to 580 nm.

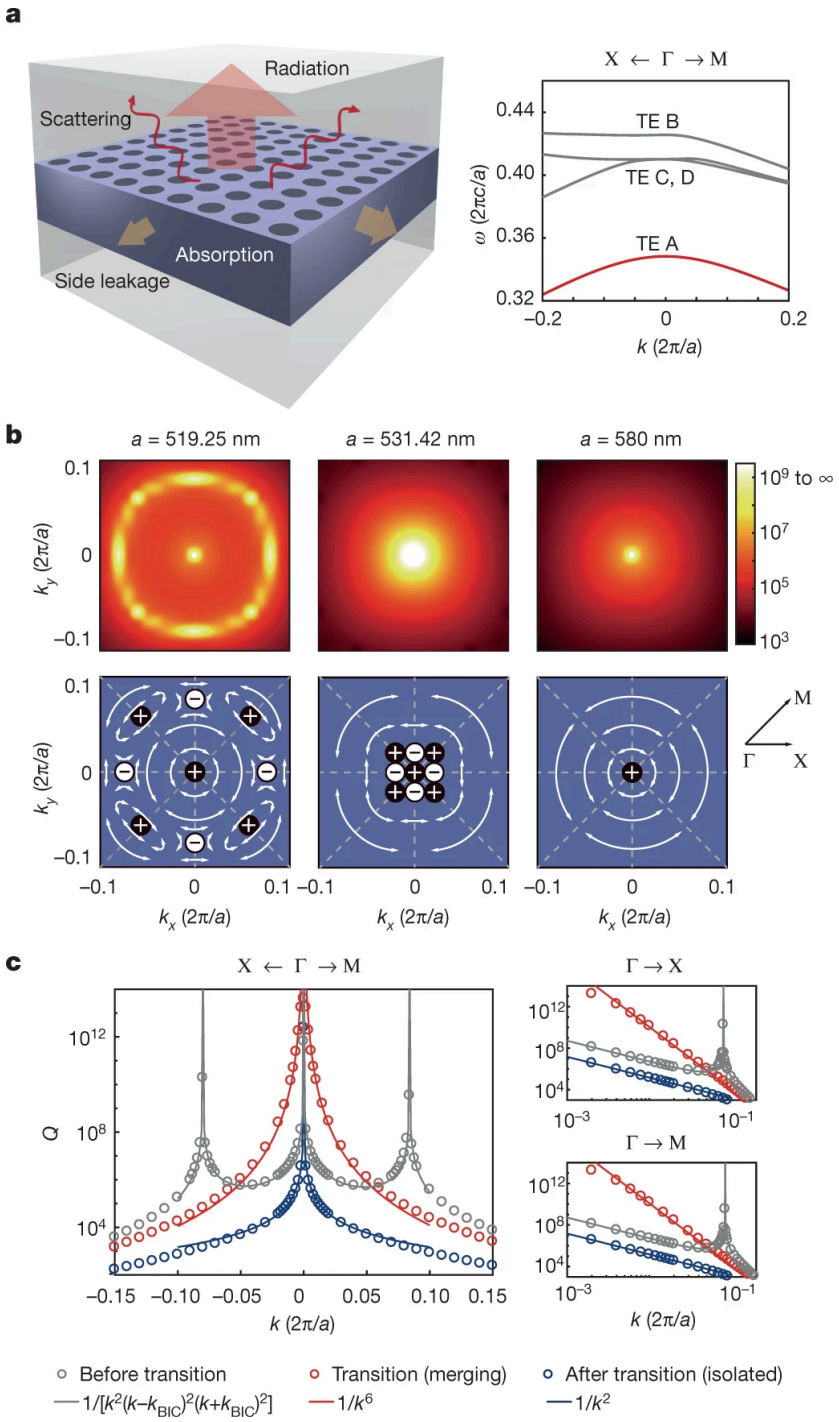

Fig. 10 a, Left, Schematic of a photonic crystal slab and the factors contributing to loss. Right, Simulated band structure. The TE A band is marked with a red line, and ω is the normalized resonance frequency. b, Multiple BICs appear on band TE A, where the radiative quality factor Q diverges. Top, Simulated Q for various values of the sample periodicity, a. Bottom, far-field polarization plots. When a is tuned from 519.25 nm (left) to 580 nm (right), nine BICs at kBICwith topological charge ±1 merge into an isolated BIC with charge +1. c, Simulated Q before (a = 519.25 nm; grey) and after charges merge at the centre of the Brillouin zone (a = 580 nm; blue). The transition (a = 531.42 nm; red) corresponds to the merging-BIC configuration, which shows considerably higher quality factors than the isolated-BIC configuration (blue). This is caused by a change to a scaling rule of $Q \propto 1/k6$, which is observed along both the Γ−X and Γ−M directions. All simulations used the finite-element method in COMSOL.

Although simulation results of infinitely large perfect photonic crystals reproduce radiative quality factors, real samples (schematically shown in Fig. 11a) feature some major differences that determine the highest *Q* achievable in practice. First, all samples are finite in size; their boundaries introduce fractional orders of the primitive reciprocal lattice in *k* space (green dots in Fig. 11a). Second, all fabricated samples exhibit disorder and imperfections with both long- and short-range correlations, allowing modes at different *k* points to couple to each other. Because of these inevitable coupling terms, modes at different fractional momentum orders are hybridized and all of their loss channels become available to the final resonance.

The advantage of our merging-BIC design over an isolated-BIC design is confirmed by simulations (using the COMSOL Multiphysics software) of perturbed 15 × 15 photonic crystal supercells. In a perfect supercell structure without disorder, a BIC with infinite *Q* remains at the centre of the Brillouin zone (Fig. 11b, upper panel). For comparison, perturbations are applied to both the radii (Δ*r*) and positions (Δ*x*, Δ*y*) of the holes according to the statistics that best describes our samples (Fig. 3). As expected, each mode in the disordered samples has multiple components in *k* space. Furthermore, resonances in a disordered sample with a merging-BIC design have considerably lower radiation fields than those from an isolated-BIC design with the same disorder (Fig. 11c). This result agrees well with Fig. 10b,c: all modes contributing to the final resonance in the merging-BIC sample have much higher *Q* values than those in the isolated-BIC case because resonances in the former are much more immune to out-of-plane scattering from disorder than in the latter.

To verify our theoretical findings, we fabricate photonic crystal samples with both merging-BIC and isolated-BIC designs using the same electron-beam lithography and inductively coupled plasma etching processes on a 600-nm-thick silicon-on-insulator wafer. The underlying SiO2 layer is then removed to restore the up–down mirror symmetry required for tunable BICs. Alternatively, one may use refractive-index-matching liquid or deposition layers instead. The samples are about 250 × 250 μm2 in size. The periodicity is varied from 530 nm to 580 nm to sample designs with merging and isolated BICs. From the scanning electron microscope images of the samples (Fig. 12a,b), the standard deviations of the hole locations and radii are estimated to be about 5 nm, which is used in the simulations discussed earlier.

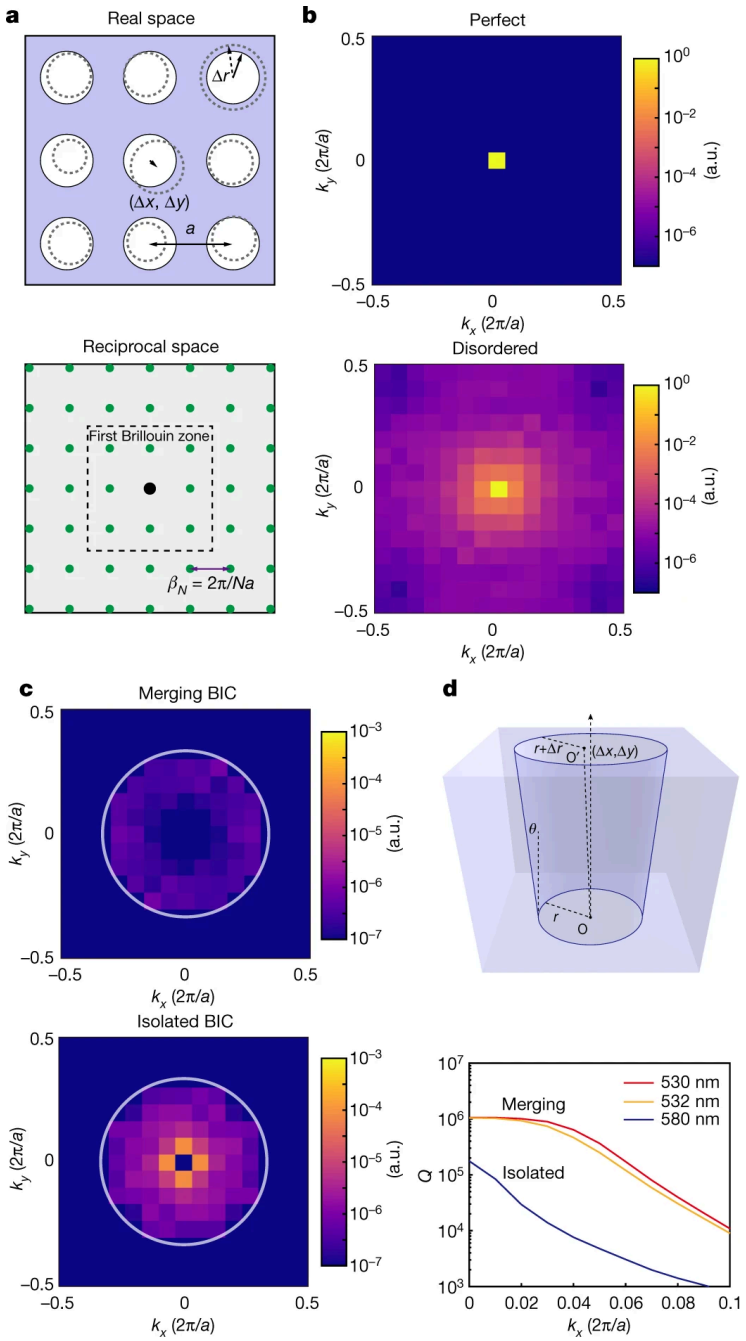

Fig. 11 a, Schematic of a fabricated photonic crystal sample (solid lines; top), with disorder in the locations and radii of the holes (dashed lines; top). In reciprocal space, fractional orders of momentum (green dots; bottom) are introduced by the supercell. *N* is the size of the supercell in increments of the periodicity *a*and *βN* is the minimum step size of the fractional orders of momentum. b, Momentum–energy distribution of the highest-*Q* mode in the merging-BIC design for a perfect (top) and a disordered (bottom) structure inside the first Brillouin zone. a.u., arbitrary units. c, Momentum–energy distribution of the radiation field in the disordered merging-BIC (top) and isolated-BIC (bottom) designs. The white circles represent the light cone—the region in the momentum space where guided resonance can couple to the radiation channel, as determined by the structure of the sample. The scattering loss is considerably lower in the merging-BIC sample than in the isolated-BIC sample. d, Schematic of an asymmetric hole (top) acting as a fabrication imperfection, and simulated *Q* values near the centre of the Brillouin zone obtained by the application of disorder (bottom). All simulations were performed in a 15*a* × 15*a* supercell (*N* = 15).

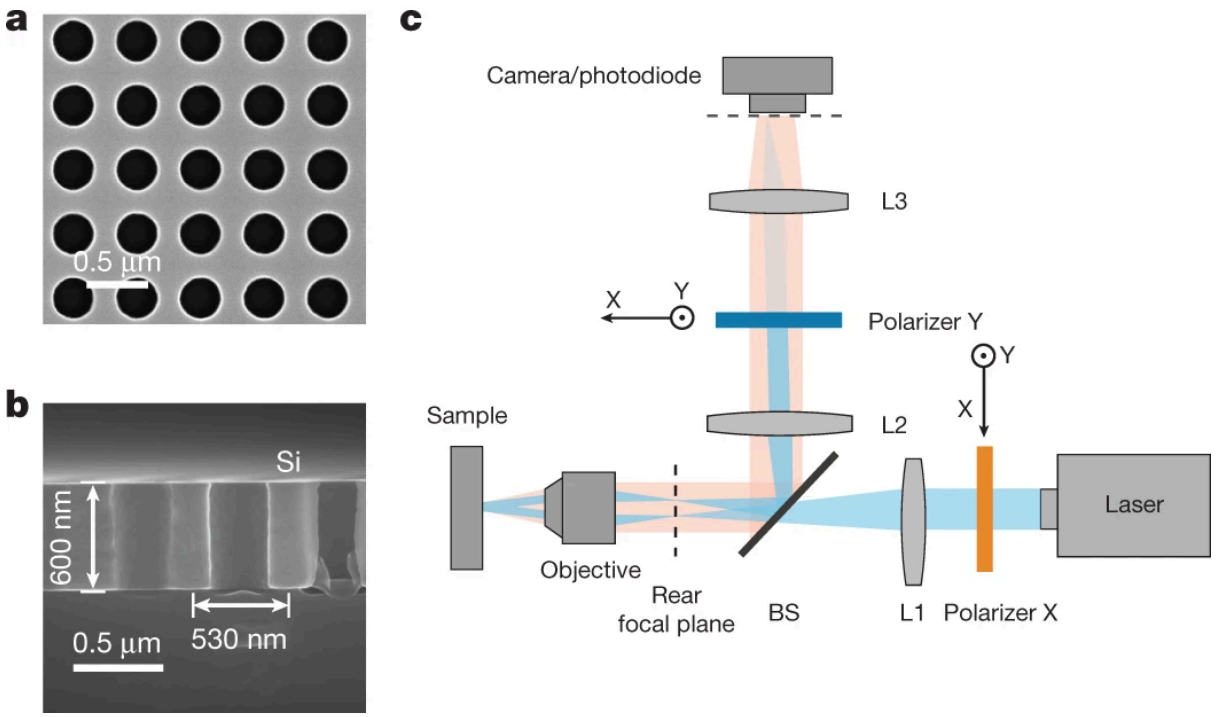

Fig. 12 a, b, Scanning electron microscope images of the fabricated photonic crystal sample; top (a) and side (b) view. c, Schematic of the measurement setup. The blue lines represent the incident light and its direct reflection. The light red region denotes radiation losses induced by scattering from disorder. L, lens. BS, beamsplitter.

A schematic of the experimental setup is shown in Fig. 12c. A tunable telecommunication laser with light in the C+L band is first sent through an X-polarizer before the light is focused by a lens (L1) onto the back focal plane of an infinity-corrected objective lens. The incident angle of the laser on the sample is thus controlled by moving L1 on the $x-y$ plane. Using this confocal setup, reflected and scattered light are also collected by the same objective; they are then magnified 1.67 times through a relay 4f system and imaged on a camera. A Y-polarizer is used to block reflected light (X-polarized) while allowing scattered light to pass. Under the on-resonance coupling condition, where the photonic crystal sample supports a resonance at the same wavelength as the incident light at that incident angle, isofrequency contours are observed on the camera, similarly to previously reported results.

The Q values of resonances at different k points are further characterized using scattered light. Specifically, a movable pinhole (not shown in Fig. 12c) is placed on the image plane of the objective's rear focal plane to specify a k point. A photodiode connected to a lock-in amplifier is placed behind the pinhole to record the intensity of the scattered light as a function of the wavelength of the tunable laser. As shown in Fig. 13a, when different k points are selected by the pinhole (X, Y and Z), different scattering spectra are obtained, all exhibiting symmetric Lorentzian

features. Similar scattering phenomena have been observed before and can be understood as follows: the intensity of scattered light is governed by the spectral density of states of the sample at that *k* point, and is described by a Lorentzian function centred at the resonance frequency, with linewidth determined by the *Q* value of the resonance.

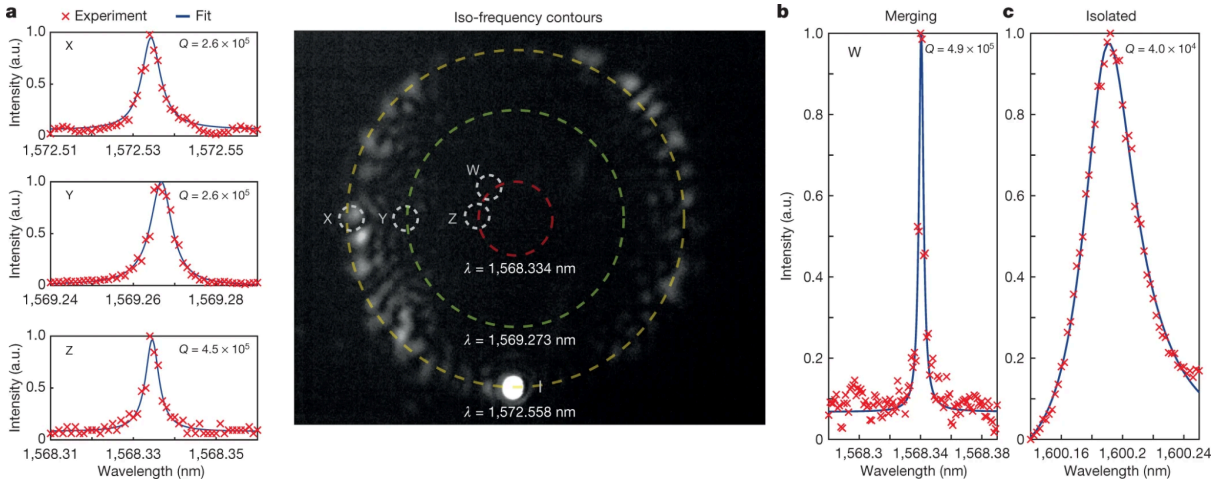

Fig. 13 a, Isofrequency contours of the sample at different wavelengths are observed on the camera (right). Three examples are shown as dashed lines. The scattered-light intensity at different points in momentum space (X, Y, Z; left) is further characterized using a photodiode, and is fitted by symmetric Lorentzians as a function of incident wavelength. The linewidth is determined by the *Q* value of the underlying resonance. b, c, The highest *Q* observed in the merging-BIC sample is 4.9 × 105 at point W (b), which is more than an order of magnitude larger than that of an isolated-BIC sample constructed with the same fabrication process (*Q* = 4.0 × 104; c).

The *Q* values of the resonances are extracted by numerically fitting the scattering spectra with Lorentzian functions. As shown in Fig. 13a, *Q* increases from 2.6 × 105 to 4.5 × 105 as the observing point moves closer to the centre of the Brillouin zone from X to Z. This agrees well with the simulation results in Fig. 10. The highest *Q* observed in the merging-BIC sample is 4.9 × 105 at point W (Fig. 13b). In comparison, the highest *Q* observed in the isolated-BIC sample—fabricated on the same wafer through the same processes as the merging-BIC sample, but with different structural parameters—is limited to only 4 × 104, more than an order of magnitude lower (Fig. 13c). This confirms our simulation results in Fig. 11, which indicate that engineering the topological configurations of BICs can substantially suppress scattering losses. Furthermore, this over-ten-fold enhancement of the quality factor is observed to be robust: not only does it appear over a wide range in *k* space, as shown in Fig. 14, but a similar level of enhancement is also observed in all merging-BIC samples that we fabricated.

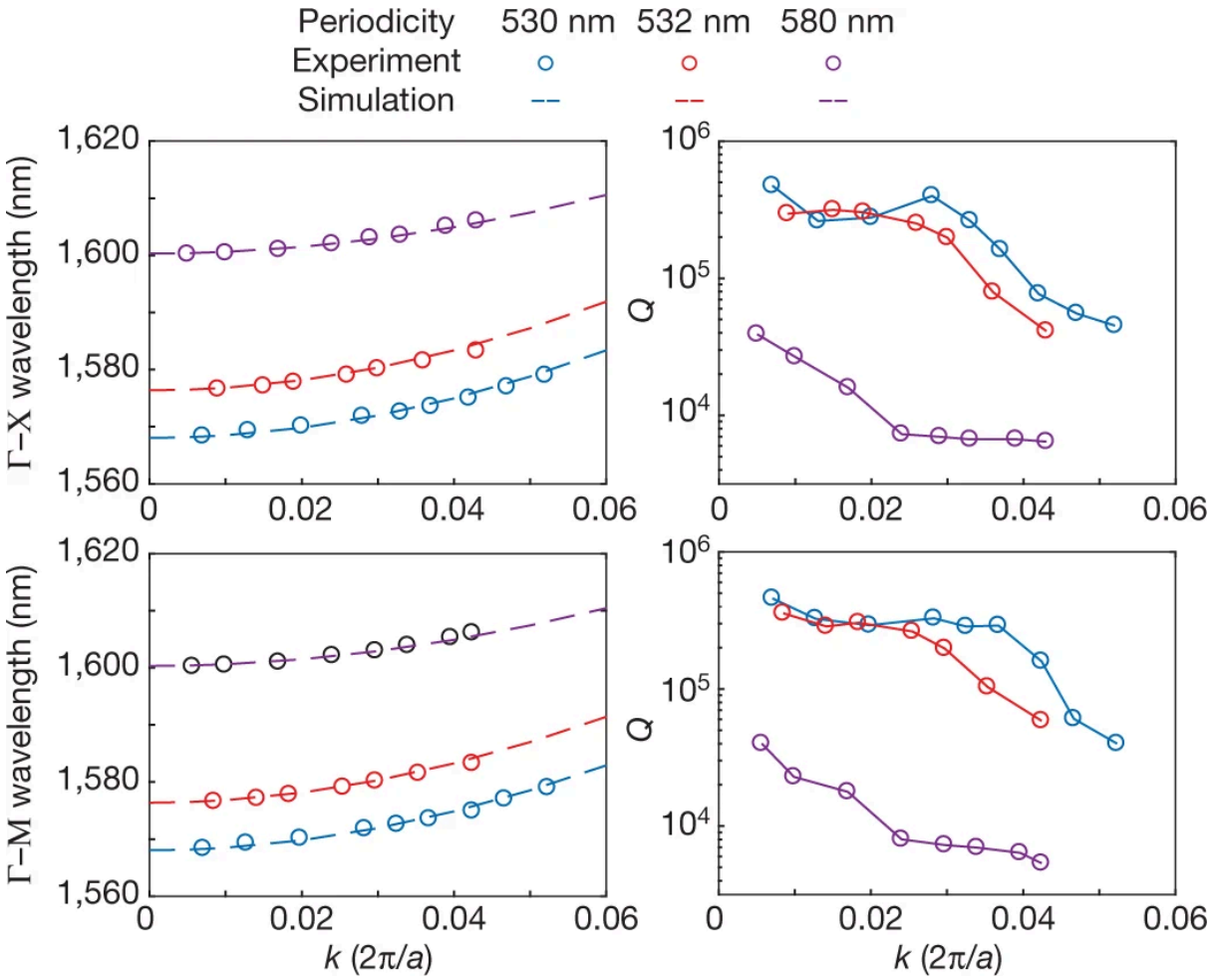

Fig. 14 a, Dispersion of resonances measured at different points in momentum space (circles), showing good agreement with FEM simulation predictions (dashed lines) along both the Γ−X (top) and Γ−M (bottom) directions. b, An enhancement of *Q* by a factor of more than 10 is observed over a wide range in momentum space for the merging-BIC samples (red and blue) compared to the isolated-BIC sample (purple) owing to topological protection.

Topological photonics has found tremendous success in suppressing in-plane back-scattering losses by breaking reciprocity. Here we use topology to solve a different class of problems, by suppressing out-of-plane-scattering losses in a reciprocal system. By merging multiple topological charges carried by BICs, we experimentally demonstrate photonic crystal resonances with record-high quality factors of $Q = 4.9 \times 105$, more than an order of magnitude higher than those of ordinary designs. These ultrahigh-*Q* resonances are potentially useful for chemical or biological sensing30 and large-area laser applications18. Furthermore, our high-*Q* resonances are observed to be robust against fabrication imperfections, and can help to improve the performance of optoelectronic devices using concepts from topological photonics.

5. Floquet topological phases in one-dimensional nonlinear photonic crystals (Phys. Rev. Lett. 126, 113901, 2021)

Our second project is to explore Floquet topological phases in driven nonlinear photonic crystals, which corresponds to non-Hermitian generalized eigenvalue problems. The non-Hermiticity comes from the non-conserving photon numbers in parametric processes (e.g., $\chi^{(2)}$ optical parametric amplifiers), not from the traditional optical gain or loss in previously studied systems.

Specifically, We report on a theoretical analysis of the Floquet topological crystalline phases in driven one- dimensional photonic crystals mediated by second-order optical nonlinearity. We define the photonic Berry connection and photonic polarization in such systems using different methods and prove their equivalence. We present two examples of topological phase transitions, when two Floquet bands cross and open new gaps under the driving field. Finally, we analyze the physical consequences of each topological phase transition by examining both edge states and filling anomalies. Our study presents routes towards realization of robust reconfigurable photonic cavities with topologically protected light confinement.

We start by formulating the Floquet eigenvalue problem and defining the 1D topological invariants. The nonlinear PhC under study is schematically shown in Fig. 15(a), which consists of alternating layers of a second-order nonlinear material, LiNbO3 with linear permittivity of εxx =εyy=4.97 and εzz =4.67,and a linear material, Si with ε=12.25. Both materials are chosen as they are commonly used in integrated photonics. In the visible/near-infrared regime of interest, LiNbO3 has a large second-order nonlinear susceptibility of χ(2) = 2d = 62 pm/V, which can lead to an appreciable Floquet gap under moderately strong driving fields. The PhC is uniform along the y and z directions and has a periodicity of a along the x direction. The width of the Si layer is w = 0.6a. The LiNbO3 is x-cut and the crystallographic c axis is parallel to the z axis as defined in the inset. In this work, only transverse- magnetic (TM) modes propagating along the x direction with field components (Ez,Hx,Hy) are considered. The static band structure of the four lowest bands and their corresponding mode profiles are calculated using a finite-element solver with the band structure shown in Fig. 1(b). The Zak phase of a TM band is defined as the integral of the Berry connection over the BZ

$$\theta_{\mathrm{Zak}} = \int_{\mathrm{BZ}} \mathcal{A}_k dk = i \int_{\mathrm{BZ}} \langle u_k^z | \, \varepsilon_{zz} \partial_k \, | u_k^z \rangle \, dk,$$

Here, *A* is the Floquet Berry connection. Next we show how topological phase transitions can be induced by external driving fields in the 1D nonlinear PhCs. A monochromatic driving field impinges from the y direction and periodically modulates the permittivity of LiNbO3 via the electro-optic effect, $\Delta\varepsilon(t) = 2\chi^{(2)}E\cos(\Omega t)$. The driven

system only has a discrete translation symmetry in time. Accordingly, each static band |j⟩ is transformed into a set of Floquet bands |j,m⟩ whose frequencies are separated by mΩ (with m an integer), as shown in Fig. 1(c).

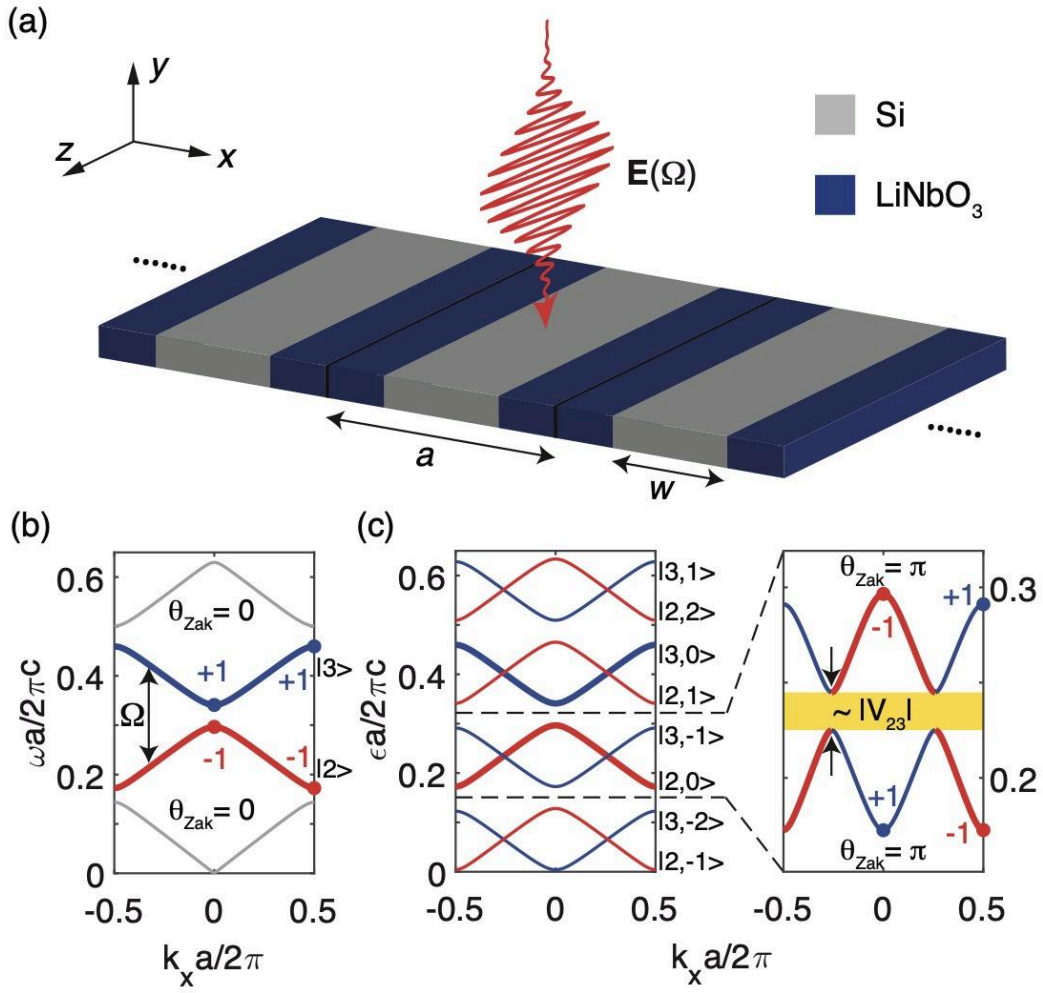

Fig. 15 Floquet topological phase transition in a driven 1D PhC. (a) Schematic of a 1D nonlinear PhC that consists of alternating layers of Si and LiNbO3. An external driving field E(Ω) couples different TM modes via the electro-optic effect of LiNbO3. (b) The dispersion of the four lowest TM bands are calculated. The second (red) and third (blue) static bands, both topologically trivial, are coupled via the external driving field. (c) Under driving, a Floquet gap is opened (yellow) and both Floquet bands have topologically nontrivial bulk polarizations.

A topological phase transition is induced by inverting Floquet bands |2, 0⟩ with |3, −1⟩. For a small driving frequency Ω, Floquet band |2,0⟩ is always at lower frequency than |3, −1⟩, separated by a quasi-energy gap. As Ω increases to the critical value of Ωc, the Floquet gap is closed at Γ, where the coupling strength V23 between the two bands vanishes due to the C2y-symmetry mismatch. As Ω further increases, the band inversion is completed, and a new Floquet gap is opened with the gap size proportional to the magnitude of the coupling strength |V23|. More importantly, both

Floquet bands become topologically nontrivial after the band inversion. The C2y indices switch at Γ, and accordingly, the Zak phases of both bands change to π, indicating a non- trivial polarization for each band. This topological phase transition is further confirmed by directly integrating the Berry connection over the BZ to calculate the Zak phase.

Next we present the physical consequences of this topo- logical phase transition from a trivial static phase to a nontrivial polarized Floquet phase. Specifically, we show that the driving field induces new edge states accompanied by an anomalous depletion/overfilling of mode densities within the bands, as schematically shown in Fig. 2(a). In the case of the trivial static phase, for a finite system with *N* unit cells, each bulk band becomes a set of N modes, representing the bulk contin- uum (schematically shown in green). Under the driving field, the bulk bands undergo a transition into the po- larized Floquet phase with nontrivial polarizations. As a result, two degenerate topological edge states emerge inside the Floquet gap, marked as red and blue circles. These two edge states have contributions from the bulk states in the bands both above and below the gap. Consequently, each bulk continuum is left with only $N-1$ states, leading to a filling anomaly that is robust against perturbations preserving C2 symmetry. In comparison, while edge states may also appear in topologically trivial systems by tuning the boundary condition, such edge states have contributions solely from the bulk states either below or above the gap, leaving $N-2$ states in the bulk continuum, and this does not lead to filling anomalies.

Overall, we analyze the Floquet topological crystalline phases in driven 1D nonlinear PhCs, which are described by generalized non-Hermitian eigenvalue problems. Through the study of two types of topological phase transitions, we elucidate the definition of topological invariants and their physical consequences in these systems. Our formalism can be further generalized to compute quadrupole moments and to study high-order topology in driven nonlinear systems. Our framework is also applicable to other nonlinear systems without particle conservation, such as phonons and polaritons. The presented 1D Floquet topological phases may en- able reconfigurable cavities with applications in on-chip Q-switch lasers and light wave-controlled strong light- matter interactions.

6. Quadrupole topological photonic crystals (Nature Communications, 11, 3119, 2020)

Our second project is to explore higher topology with quantized topological invariants in photonic crystals. Quadrupole topological phases, exhibiting protected boundary states that are themselves topological insulators of lower dimensions, have recently been of great interest. Extensions of these ideas from current tight binding

models to continuum theories for realistic materials require the identification of quantized invariants describing the bulk quadrupole order. Here we identify the analog of quadrupole order in Maxwell's equations for a gyromagnetic photonic crystal (PhC) through a double-band-inversion process. The quadrupole moment is quantized by the simultaneous presence of crystalline symmetry and broken time-reversal symmetry, which is confirmed using three independent methods: analysis of symmetry eigenvalues, numerical calculations of the nested Wannier bands and the expectation value of the quadrupole operator. Furthermore, we reveal the boundary manifestations of quadrupole phases as quantized edge polarizations and fractional corner charges. The latter are the consequence of a filling anomaly of energy bands as first predicted in electronic systems.

Recently, quadrupole TIs have been demonstrated in a number of classical systems, ranging from microwave and optics to acoustics and circuits. Most experiments are analyzed as lattice models, following the tight-binding approximation. In these lattice models, the adopted symmetry required to quantize the quadrupole moment is reflection or fourfold rotation ($C4$) with threaded π-flux, and hence these systems are time-reversal invariant. Unfortunately, most realistic systems with subwavelength features, such as photonic crystals, cannot be modeled discretely but require a different continuum approach. For example, the practical implementations of many lattice models no longer preserve quantized bulk quadrupole moments in the continuum theory. In addition, most experimental works solely used the existence of in-gap corner states as the measure of bulk quadrupole topology. The validity relies on the presence of additional chiral symmetry in the lattice model, which is often not preserved in the continuum theory.

Here, we find solutions to continuous Maxwell's equations in gyromagnetic photonic crystals that are the electrodynamic analogs to quadrupole topological phases. The proposed topological PhCs have quantized bulk quadrupole moments, which are protected by the simultaneous presence of crystalline symmetries and broken time-reversal symmetry (T). In particular, we show it is essential to break time-reversal symmetry—to open the energy gap—while preserving crystalline symmetries—to quantize bulk dipole and quadrupole moments. In addition, we note the existence of corner states is neither sufficient nor necessary for quadrupole phases. Instead, we validate the bulk quadrupole nature through analyzing the Wannier band polarization and its manifestations at boundaries as quantized edge polarizations and fractional corner charges. All calculations are based on realistic parameters that are readily available in the microwave regime.

We start by presenting the topological phase transition between a trivial (Fig.1b) and a quadrupole two-dimensional (2D) PhC (Fig.16c). The 2D PhC consists of gyromagnetic rods in air and is homogeneous along the out-of-plane (z) direction. Experimentally, this boundary condition can also be realized using metals.

The gapless transition point is achieved in a 2 × 2 super-cell structure with four square rods (Fig.1a). All rods are identical in shape and are of the same gyromagnetic material of Yttrium Iron Garnet (YIG) with isotropic dielectric permittivity of $\epsilon = 15\epsilon 0$ and inplane permeability $\mu = 14\mu 0$. To break time-reversal symmetry, an external magnetic field is applied along the out-of-plane direction (z), which induces complex-valued off-diagonal terms in the permeability tensor of YIG:

$$\bar{\bar{\mu}} = \begin{bmatrix} \mu & i\kappa & 0 \\ -i\kappa & \mu & 0 \\ 0 & 0 & \mu_0 \end{bmatrix}$$

Here the gyromagnetic response, κ, breaks T but preserves $C4$ and $Mx(y)T$. Here $Mx(y)$ is the mirror reflection that transforms $x(y)$ to $-x(y)$. At the phase transition, all rods are placed at $a/2$ away from their neighbors; the corresponding band structure for TM modes (Ez, Hx, Hy) has twofold (fourfold) degeneracies at the center (corner) of the folded Brilluion zone Γ(M). Both degeneracies are lifted when the four rods are simultaneously displaced inward ($d < 0$, Fig. 1b) or outward ($d > 0$, Fig. 16c) along the diagonal lines of the unit cell. On either side of the transition point, the band structure is fully gapped owing to T-breaking (shaded in yellow) and supports two topologically distinct phases determined by the displacement d: for the choice of cell in Fig. 1, inward displacements with negative d give rise to trivial phases, whereas outward displacements with positive d correspond to quadrupole phases.

To confirm the quadrupole topology of our PhC, we explicit show that its dipole moments are zero ($px = py = 0$), but its quadrupole moment is non-zero ($qxy = 1/2$). To this end, we perform two separate sets of calculations using two different methods: (1) the nested Wilson loop formulation; (2) and the expectation value of the exponentiated quadrupole operator, and show they reach the same conclusions. Here, we present the nested Wilson loop calculations. We start by computing the band structure and mode profiles (Ez) of the TM modes for a particular displacement of dielectric rods $d = a/4 - w/2$ (Fig. 3a, same as in Fig. 2c). Using these as input, we compute the Wannier bands vx,y for the two lowest-energy bands.

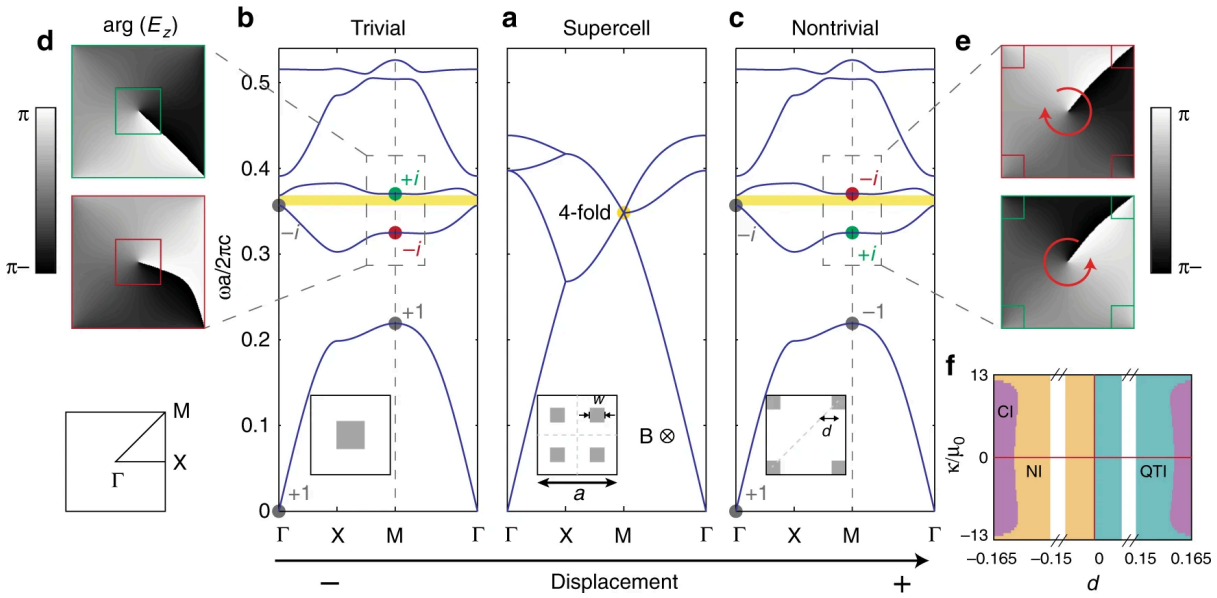

Figure 16. Band degeneracies are created at the center (Γ) and corner (M) of the folded Brilluion zone for a 2 × 2 super-cell PhC (inset). An external magnetic field (B) induces gyromagnetic responses in YIG rods (gray squares), which breaks *T* but preserves *C*4. The gyromagnetic response $\kappa = 12.4\mu 0$ is used in the calculations. b, c As the rods simultaneously move inward or outward, the second gap is opened (shaded in yellow), but with different quadrupole phases: inward (outward) displacements with negative (positive) *d* correspond to trivial (non-trivial) quadrupole phases. d, e *Ez* mode profiles for the second and third modes at M feature a band inversion between the modes with *C*4 index of +*i* (green) and −*i* (red) in the trivial and non-trivial phases. f Complete topological phase diagram of the PhCs, including quadrupole phases (green), trivial phases (orange), and Chern insulating phases (purple).

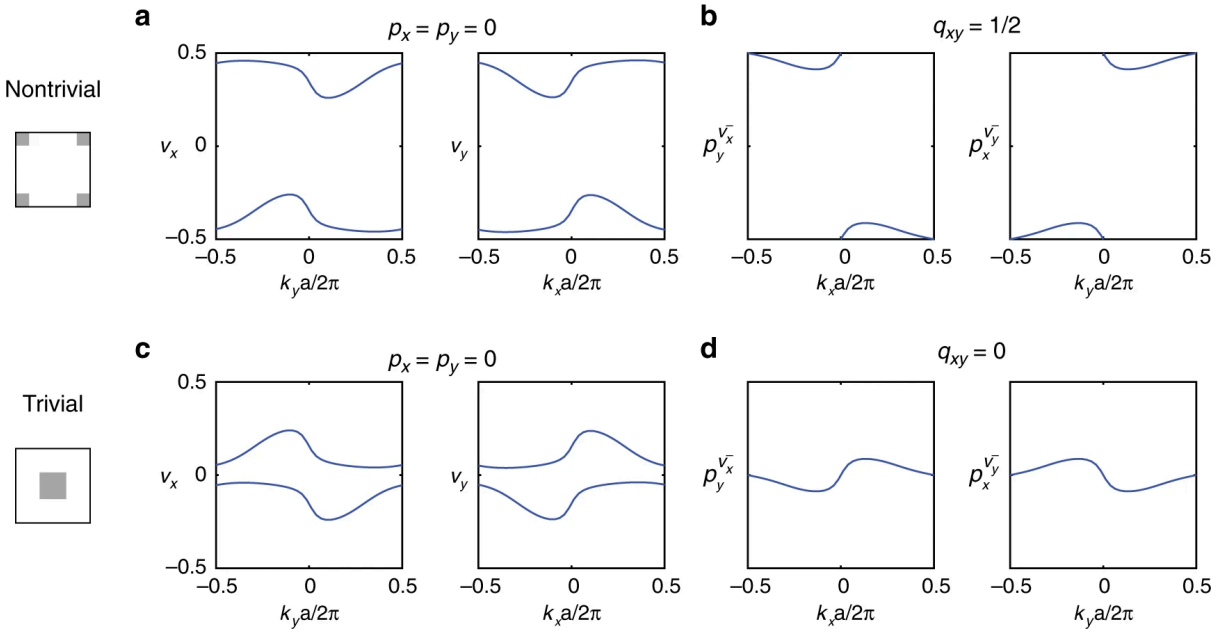

Figure 17. Wannier bands, *vx*(*ky*) and *vy*(*kx*), are calculated for the first and second bands of the quadrupole PhC. Results show the bulk dipole momentum is zero (*px* = *py* = 0). b Calculations of the nested Wilson loops, , show the bulk quadrupole momentum *qxy* is non-trivial and quantized to 0.5. c, d Similar calculations repeated for a trivial PhC, showing zero bulk dipole moments (*px* = *py* = 0) and zero quadrupole moments.

To compare, we repeat the same set of calculations for a different unit cell with a negative displacement of $d = -(a/4 - w/2)$ (Fig. 3c). As shown, the Wannier bands are also gapped and sum to zero, meaning the bulk dipoles *px*,*y* remain zero. However, the nested Wilson loops, and , are also zero, leading to a trivial quadrupole moment $qxy = 0$. This correspondence between positive (negative) displacements leading to non-trivial (trivial) quadrupole phases is consistent with our preceding conclusions based on *C*4 symmetry eigenvalues. Importantly, the non-trivial and trivial PhCs in Fig. 3 can be simply related to each other, by shifting the choice of the unit cell center by *a*/2.

Finally, we show the physical consequence of quadrupole PhCs as localized 0D corner states, which are the photonic analogs of states responsible for filling anomalies and fractional charges in an electronic setting. To this end, we solve the eigenstates in a finite 2D quadrupole PhC enclosed by PECs, with a thin air gap in between (Fig. 4a). The eigenstates are labeled according to their energies, with the lowest-energy state labeled as 1. Aside from delocalized bulk states, four degenerate states—199 through 202—are found, with their energies inside the bulk energy gap (Fig. 4b). Their mode profiles (*Ez*) confirm that these states are spatially localized at the four corners, with one example shown in Fig.4c. Owing to the lack of chiral symmetry in our system, which is generic in the continuum theory expanded around non-zero frequencies, the energy of the four corner states is not pinned at the center of the bulk energy gap; instead they can be shifted, even immersed into the bulk continuum, by modifying the refractive index at the corners. This renders the appearance of corner states less of an essential signature of quadrupole phases. In fact, corner states are also found in other higher-order topological phases with vanishing bulk quadrupole moments.

Instead, here we illustrate the non-trivial quadrupole nature of our PhC using the filling anomaly, by counting the number of energy eigenstates below and above a given bulk energy gap (Fig. 4a). Specifically, even though trivial samples may support corner states, they originate from either the top or bottom band alone, leaving $2N2-4n$ states in the bulk continuum (*n* is an integer). On the other hand, for non-trivial PhCs, the number of states below and above the energy gap are both $2N2 - 2 = 198$ ($N = 10$ in our case). This indicates the four degenerate corner states we observed are “contributed” by both the top and bottom bands together, and thus proves the non-trivial quadrupole topology of our design. As a consequence, for a quadrupole PhC, quantized fractional charges appear at four corners of a finite sized

system (Fig. 4d) when calculate the spatial distribution of the lowest 200 energy states, in a similar vein as the calculations of charge density in electronic systems at “half-filling” (here, we have introduced an infinitesimal perturbation to break *C*4 symmetry in order to split the fourfold degenerate corner states). Remarkably, these corner charges are shared by two convergent dipoles on the two perpendicular edges, as the magnitude of the corner charges is equal to the edge polarizations. This further confirms that these corner charges originate from a non-zero bulk quadrupole moment. We point out that the observed fractional corner charges arise from the fundamental difference in the counting of bulk states, and was recently proposed in electronic systems as a filling anomaly: a mismatch between number of states in an energy band and the number of electrons required for charge neutrality.

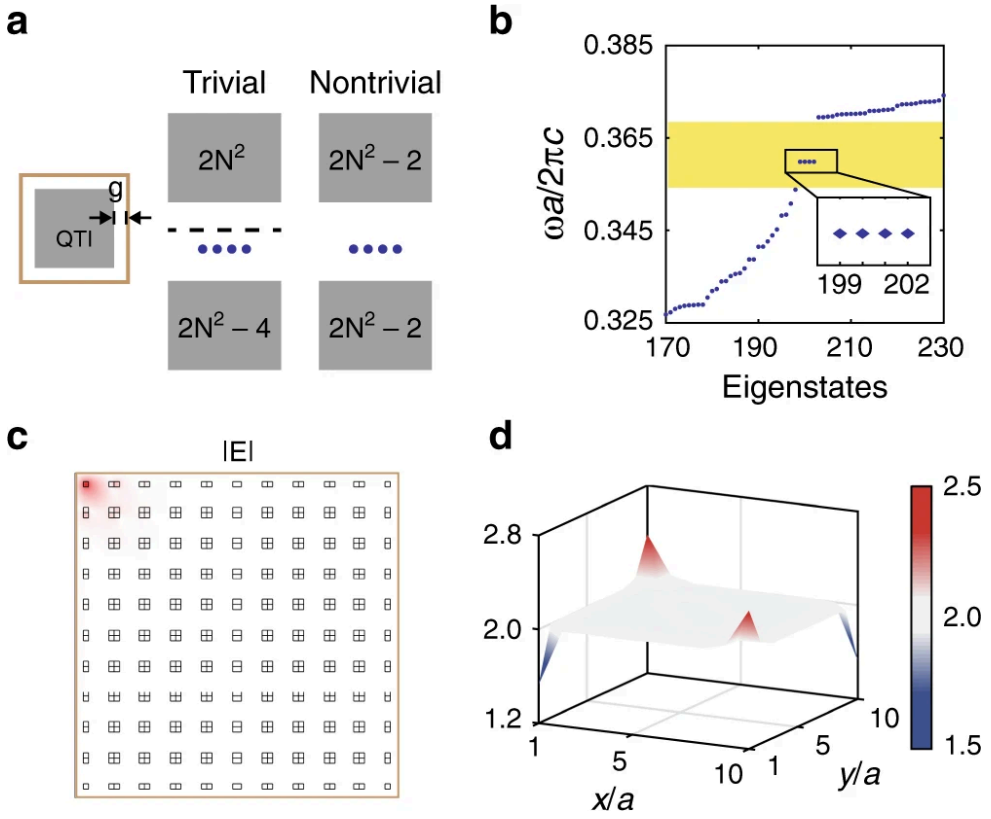

Figure 18. a For a finite PhC with *N*×*N* unit cells enclosed by PECs, the counting of the number of eigenstates below and above an energy gap are distinct between quadrupole and trivial phases. b Eigenstates of a 10 × 10 quadrupole PhC, showing four degenerate corner states inside the bulk gap, shaded in yellow. cMode profile ($|Ez|$) of one of the corner states. d Spatial distribution of the accumulative electromagnetic energy density for the lowest 200 energy eigenstates in the quadrupole PhC, showing fractional occupations (2 ± 0.5) at the corners.

In summary, we present quadrupole topological photonic crystals with truly quantized invariants and the physical consequences at material’s edges and corners. The proposed gyromagnetic PhCs can be readily realized in the microwave regime. Meanwhile, the coexistence of multiple topological phases in our system, both quadrupole TIs and Chern insulators, provides a versatile platform to further

demonstrate topological photonic circuits with protected elements immune to disorders in various dimensions. Finally, our findings of inducing quadrupole phase transitions and quantizing quadrupole moments—through crystalline symmetries in conjunction with broken time-reversal symmetry—can also be applied to other wave systems, including electrons, phonons, and polaritons.